Numerical Simulation of Internal Tides and Comparison to Observation

by

Kehan Li

A thesis submitted in partial fulfillment of the requirements for the degree of

Master of Science

Department of Earth & Atmospheric Sciences
University of Alberta

Abstract

As internal tides propagate in the ocean, they carry and dissipate energy over hundreds and even thousands of kilometers. We perform fully nonlinear simulations to examine the evolution of horizontally propagating, vertical mode-1 internal tides in non-uniformly stratified fluids, as it depends on wave amplitude, ocean depth, Coriolis forces, and the spanwise extent of the waves. The background stratification is set up according to ocean measurements southwest of Hawaii and in the South China Sea. Two-dimensional (2D) simulations on the β-plane are based on the internal tides originating near the Hawaiian Ridge and propagating southwest towards the equator. The results are compared to the ocean measurements from the EXperiment on Internal Tidal Scattering (EXITS). Another series of 2D simulations on the f-plane is set up based on the internal tides propagating westward in the South China Sea and are compared to the observations. The simulations in both research domains align qualitatively and somewhat quantitatively with the observations. A three-dimensional (3D) model simulating spanwise-localized waves is utilized to characterize the evolution of internal tides in the streamwise and spanwise direction. The spanwise evolution of the 3D waves is examined in terms of the lateral spreading, radius of curvature, and sea surface signature. The evolution of sea surface signature is compared favourably to a satellite image in the South China Sea. The 3D model can thus be used to reversely deduce the initial conditions of internal tides.

Acknowledgement

First of all, I want to express my deepest gratitude to my supervisor, Bruce Sutherland, for his patient guidance throughout the project. I would not have gotten far without his support. He kindly guided and encouraged me when I was stuck in progress. His insightful and helpful feedback helped me to grow both professionally and personally. I am sincerely thankful for the opportunity to learn and work under his mentorship. I also want to thank Paul Myers and Morris Flynn for being my supervisory committee members and giving helpful suggestions at the committee meeting.

I want to thank my fiancée, Xiner Wu, for the invaluable emotional support she provided during this process. Her love, patience, understanding, and unwavering belief in my abilities have been a constant source of strength, helping me to overcome the various challenges I faced. I also want to thank my parents for supporting and encouraging me throughout my Master's study. Particularly as I transitioned from another country, the support and encouragement from my loved ones have been invaluable to me.

To my dear lab mate, Alain Gervais, thank you for helping me out when I had trouble in my coding. Alain, you're such an expert in super-computing. I would like to thank Adam Fu, Tahya Weiss-Gibbons, Pouneh Hoshyar, Mohnish Kapil, and Rowan Brown. Thank you guys for the company in our numerical lab and I appreciate the fun times we spent together. I also want to thank Akash Kav, Diego Martinez, and Dennis Thai for their helpful questions and feedback at the group meetings. I am also deeply grateful to my close friends, Guofeng Lin, Vivek Kumar, Yeshe Hoffmann, and Yibo Tang. Your companionship, laughter, and support have truly enriched my life during this journey.

Contents

List of Tables

List of Figures

Chapter 1

Introduction

1.1 Internal tides

1.1.1 Internal gravity waves in the ocean

Oceans, in general, are stably and continuously stratified fluids with mean profile of density increasing with depth primarily due to a decrease in temperature and an increase in salinity with depth (e.g. Vallis, 2017). Such fluids support internal waves, which are driven by buoyancy forces, as illustrated by the motion of a fluid parcel. A fluid parcel is an infinitesimal volume of fluid. In a stably stratified fluid, a fluid parcel experiences a restoring buoyancy force when displaced from its vertical position into surrounding fluid with different density. Upon returning to its level of neutral buoyancy, due to its momentum it overshoots its equilibrium position once again experiencing a restoring buoyancy force. Thus the fluid parcel oscillates in time. Collectively, this oscillation is manifest as an *internal (gravity) wave* that moves within a fluid. Internal gravity waves generally propagate both horizontally and vertically through the fluid, which allows momentum and energy transport in both directions over large spatial extents (Sutherland, 2010). Internal waves cause significant vertical displacements of density surfaces by tens and even hundreds of meters in the ocean interior in some locations such as near the Hawaiian ridge (e.g. Klymak et al., 2008; MacKinnon et al., 2017) and in the South China Sea (e.g. Farmer et al., 2009; Huang et al., 2016). These displacements have substantial influence on the ocean's density structure, circulations, sediment transport,

nutrient supply and so on (e.g. Garrett and Kunze, 2007). The breaking of internal waves is also a main mechanism for diapycnal mixing in the open ocean (Laurent and Garrett, 2002). Furthermore, internal waves serve as a mechanical mixing source in the deep ocean, which is necessary in the large-scale ocean circulation such as the meridional overturning circulation (Munk and Wunsch, 1998). Therefore, internal waves are a key component of the ocean's dynamics.

1.1.2 Barotropic and baroclinic tides

Internal waves can be generated by any perturbation that displaces fluid parcels from their equilibrium positions in the ocean, including forcing by winds from the surface and flows interacting with bottom topography (MacKinnon et al., 2017; Morozov, 2018). The latter flows can come from tidal forcing. Barotropic tides (also known as surface tides) are large-scale surface waves commonly associated with the periodic rise and fall of sea levels due to the gravitational forces of the Moon and the Sun. They propagate as horizontally long waves in the ocean with wavelengths typically ranging from hundreds to thousands of kilometres. It is estimated that 3.5 TW of the 3.7 TW of global tidal energy is dissipated in the ocean with 1 TW of the tidal power being converted into internal (baroclinic) tides (Munk and Wunsch, 1998; Wunsch and Ferrari, 2004; Garrett and Kunze, 2007). *Internal tides* are internal waves in the ocean generated by surface tides moving the stratified ocean water over sloping topography (e.g. Sutherland, 2010). After being generated at the topography, they can be decomposed into the vertical basis modes, with the lowest mode 1 and possibly higher modes. Low modes have a relatively large vertical length scale and are observed to propagate far away from the topography (e.g. Ray and Mitchum, 1997). On the other hand, higher modes, having a relatively small vertical length scale, exhibit slower propagation and tend to dissipate locally (e.g. Klymak et al., 2012). The steepness of the submarine topography has a major influence on the generation of internal tides by controlling the amount of energy transferred from surface tides to internal tides (Garrett and Kunze, 2007). Low modes dominate when internal tides are generated over moderate topography (Echeverri et al., 2009). If the topography is sufficiently steep, vertically propagating beams associated with higher modes are launched near the topography (e.g. Pétrélis et al., 2006). These beams can cause dramatic vertical

displacements, leading to strong local turbulent mixing (e.g. Rudnick et al., 2003; Vic et al., 2019). Furthermore, these beams are observed to transform into low-mode internal tides (dominated by mode 1) after interacting with the near-surface stratification (Martin et al., 2006). Though partially dissipated by local mixing, most of the energy fed into internal tides is transported away from the topography by the low-mode waves, mostly by mode-1 waves (e.g. Echeverri et al., 2009). It was estimated that near the Hawaiian ridge 74% of the internal tide energy is radiated away from the generation site as low-mode waves (Klymak et al., 2006; Carter et al., 2008). These low-mode waves can propagate horizontally over thousands of kilometers away from their generation site (e.g. Simmons et al., 2004). Therefore, tidal conversion makes a crucial contribution on the formation of internal waves in the ocean.

1.2 Observations of internal tides

1.2.1 Hawaii Ocean Mixing Experiment

Through a campaign known as the Hawaii Ocean Mixing Experiment (HOME), barotropic (surface) tides were observed to convert to baroclinic (internal) tidal beams near the Kaena Ridge of Hawaii and then emanate as low-mode internal tides further from the generation site (e.g. Rudnick et al., 2003). The Kaena Ridge is a relatively isolated and steep submarine hill. The currents generated by the semidiurnal barotropic tides are nearly orthogonal to the topographic feature of the ridge. These set the stage for intense conversion from barotropic tides to baroclinic tides. As a part of HOME, measurements were taken at the "Nearfield" (21.68°N, 158.63°W) and "Farfield" (18.39°N, 160.70°W) sites, located at the southwest edge of the Kaena Ridge and approximately 450km southwest of the Kaena Ridge, respectively (Rainville and Pinkel, 2006). Their locations are marked by stars in Figure 1.1, with the black arrows indicating the energy flux associated with the baroclinic tide. At the Nearfield site, observations revealed vertically propagating beams, which caused substantial vertical displacement of density surfaces, leading to intense ocean mixing. At the Farfield site, vertically low-mode, horizontally propagating internal tides were observed. Particularly at the semidiurnal frequency of the lunar (M_2) tide, the energy flux displayed strong signals of these low-mode internal tides, with vertical mode-1 waves predominating. These waves further

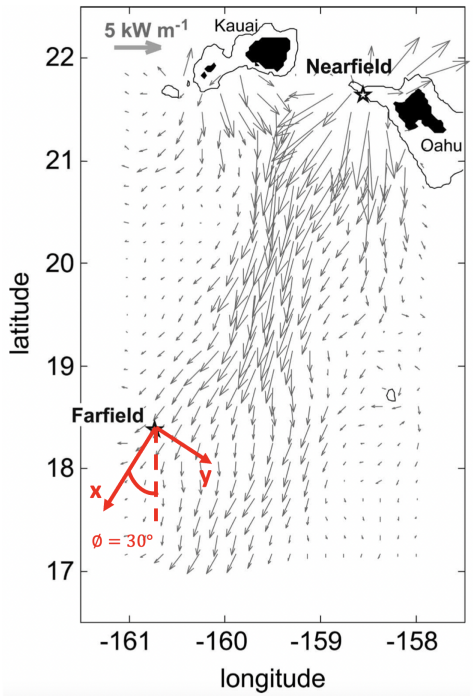

Figure 1.1: Location of the Nearfield and Farfield observation sites (stars) near the Hawaiian Ridge. Black arrows indicate the energy flux associated with the baroclinic tide (Rainville and Pinkel, 2006). Red arrows indicate the new along-wave and spanwise coordinate system for the β-plane approximation used in this thesis.

propagated south-westward towards the equator, which inspires one of the interests of this study on the behaviour of internal tides travelling towards the equator, where Coriolis forces become negligible.

1.2.2 EXperiment on Internal Tidal Scattering

The EXperiment on Internal Tidal Scattering (EXITS) examined how mode-1 internal tides originating at the Hawaiian Ridge scatter into higher-mode waves at the Line Islands Ridge, situated about 1000km southwest of Hawaii (location shown in Figure 1.2). The unpublished dataset gathered from these observations was provided by Shaun Johnston, Scripps Institution of Oceanography.

The moorings were deployed at multiple locations near the Line Island Ridge from UTC November 26th to December 19th, 2010. The locations are denoted by crosses in Figure 1.3. The arrows in Figure 1.3 indicate the depth-integrated energy flux from the M_2 baroclinic tide, with total energy flux and energy fluxes from different modes shown separately. Vertical mode-

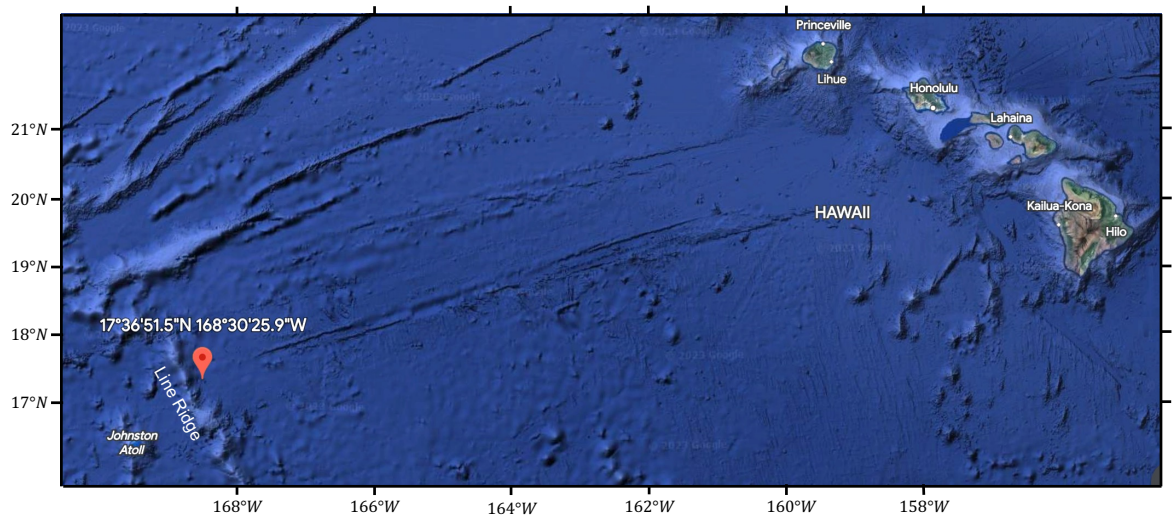

Figure 1.2: Location of ocean measurements from EXITS marked by a red pin (Image from Google Earth).

1 waves originating from the Hawaiian Ridge were observed on the north (upstream) side of the ridge. However, after they encountered the Line Island Ridge, the mode-1 waves appeared to be weaker and the mode-2 waves became the dominant signal in the observations. This was hypothesized to be due to the scattering effects occurring at the ridge (Shaun Johnston, personal communication), a phenomenon not considered in this thesis.

1.2.3 South China Sea

The South China Sea is another marine basin where internal tides exhibit substantial activity (e.g. Alford et al., 2015). The most powerful internal tides ever recorded were observed in the South China Sea (Guo and Chen, 2014). It is estimated that a total of 24GW of energy from the barotropic tides is converted into baroclinic (internal) tides at the submarine ridges in the Luzon Strait. About 40% of this energy is dissipated locally by turbulent mixing (Alford et al., 2015). The higher local dissipation rate in the South China Sea, compared to that in Hawaii, may be attributed to modelling errors (Alford et al., 2015), more complex bottom topography in the Luzon Strait (Garrett and Kunze, 2007; Buijsman et al., 2010), and the westward propagating branch of the Kuroshio (Buijsman et al., 2010). The remaining energy radiates away, mostly carried by internal tides which propagate westward across the South China Sea towards the continental shelf of China. These waves are observed to be dominated by a mode-1 signal having a combination of semi-diurnal and diurnal frequencies (Farmer

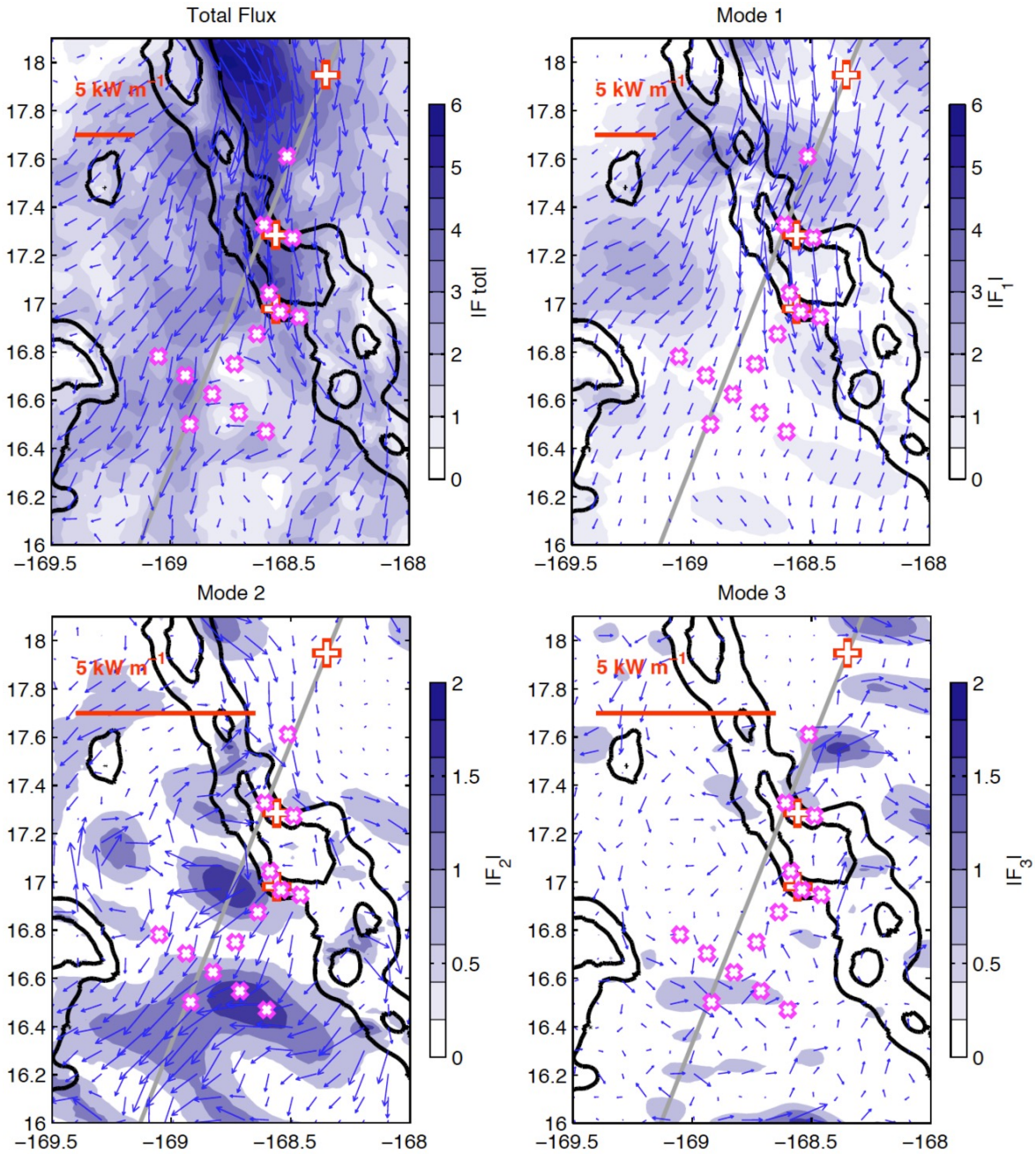

Figure 1.3: Depth-integrated energy flux from the M_2 baroclinic tide: the total flux and decomposed flux into vertical modes 1, 2, and 3. Survey stations (magenta crosses), mooring locations (red crosses), and Topex/Poseidon track 125 (grey line) are shown. Coloured contours indicate flux magnitude. (From EXITS report provided by Shaun Johnston, Scripps Institution of Oceanography)

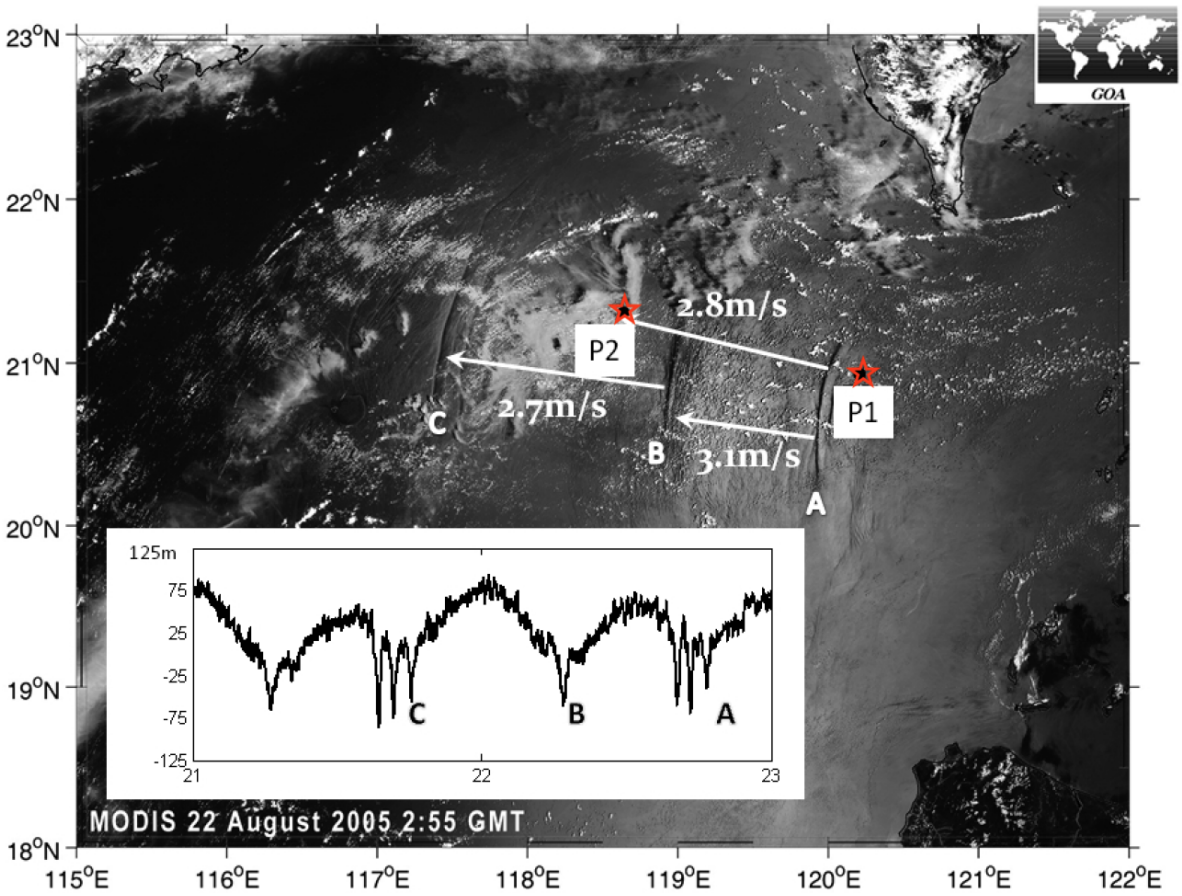

Figure 1.4: MODIS image showing three nonlinear internal wave trains (labelled by A, B, and C) crossing the deep basin west of Luzon Strait. Ocean measurements were collected at the P1 and P2 locations indicated by red stars. Inset: Corresponding inverted echo-sounder time series for these waves at P2 from which path-averaged wave speeds are determined. 122°E is the estimated generation site of internal tides in the model of 2D-forced waves. (Image reproduced with permission from Farmer et al. (2009))

et al., 2009; Johnston et al., 2013). If the semi-diurnal forcing is stronger, the internal tides tend to steepen during their propagation to form solitary waves which are visible by the sea surface signature in satellite images. Figure 1.4 shows the propagation of internal solitary waves as revealed by their surface signature seen by satellite. Given the challenging operating conditions in the Luzon Strait, as noted by Alford et al. (2015), in-situ observation data from the generation site has been notably scarce. Hence, the initial wave amplitude and the precise location of the generation site remain barely known. We assume that the generation site is along 122°E in our numerical models (detailed in Chapter 3).

1.3 Energy dissipation by low mode internal tide

Low-mode internal tides usually have large horizontal spatial extent on the order of a hundred kilometres. They carry energy as they propagate horizontally through the ocean. The energy associated with internal tides eventually converts to smaller scale, ultimately resulting in turbulent mixing (MacKinnon et al., 2017). However, it is still an open question how the energy of internal tides converts from large to small scales where turbulent mixing acts to dissipate energy, thus closing this branch of the energy budget in the ocean.

As recently reviewed by Varma et al. (2022) and MacKinnon et al. (2017), some mechanisms for the energy transformation to small scale have been proposed, such as interaction with topography and wave-wave interactions known as triad resonant instability (TRI) (e.g. Sonmor and Klaassen, 1997; Dauxois et al., 2018). Triadic resonance is a mechanism in which energy in the "parent" internal tide is transferred into subharmonic waves whose frequencies and wavenumbers sum to equal those of the parent. The theory for TRI has been widely investigated in uniformly stratified fluids, but this is not the case for the non-uniformly stratified ocean. This may explain why observations of TRI are inconclusive, as in the northeastern South China Sea (e.g. Xie et al., 2011) and to the northeast of the Hawaiian Ridge (e.g Alford et al., 2007).

Recent studies have established another mechanism by which energy can transfer to small scale. Internal waves in non-uniform stratification can self-interact to excite superharmonic waves with double the horizontal wavenumber (half the wavelength) (Sutherland, 2016; Baker and Sutherland, 2020). Under certain conditions, the excited superharmonics may successively excite higher order superharmonics with triple the horizontal wavenumber, and so on. This is referred to as the *superharmonic cascade* (SHC) (Sutherland and Dhaliwal, 2022). The excited superharmonics can also interact with the primary wave to alter its amplitude. Through this process, energy in the low-mode internal tide is converted into smaller and smaller scales. This theory will be explained in detail in Section 2.3. Although the superharmonic excitation is difficult to reveal in the ocean measurements, the superposition of the superharmonic waves results in solitary wave trains which are possible to observe by in-situ observations and satellite images.

1.4 This work

Previously, the theory and simulations of SHC were restricted to two dimensional periodic internal tides on the f-plane, for which the influence of Coriolis forces was treated as constant (Sutherland, 2016; Baker and Sutherland, 2020; Sutherland and Dhaliwal, 2022). However, the theory predicts that SHC behaves differently depending on the magnitude of the Coriolis force. Solitary wave trains resulting from the superposition of the superharmonic waves develop more rapidly with small Coriolis forces. This thesis is focused upon extending the simulations of the SHC theory to more realistic circumstances by examining their evolution on the f-plane and β-plane as they propagate from a localized forcing region. We also study three-dimensional (3D) effects associated with the internal tides having finite spanwise extent. The formation of solitary wave trains is examined as it depends on wave amplitude, ocean depth, Coriolis forces, and the spanwise extent of the waves. We adopt the South China Sea and the ocean southwest of Hawaii as the research domains in our numerical models. The models use the background stratification based on the ocean measurements in the respective domains. Simulation results are compared to in-situ observations and satellite images.

The equations of motion and theory for internal tides are described in Chapter 2. The numerical models and analysis methods used in this thesis are introduced in Chapter 3. The 2D and 3D simulation results from those models are presented in Chapter 4 and 5, respectively. Lastly, discussion and conclusions are given in Chapter 6.

Chapter 2

Theory

This chapter lays the groundwork for the theory used in this study. Section 2.1 introduces the equations of motion and the approximations applied in this study. In Section 2.2, the background stratification profiles for the two ocean domains, South China Sea and Hawaiian Ocean, are constructed based on the observed stratification, to be used in the numerical simulations. Section 2.3 reviews the superharmonic cascade theory (SHC) and its predictions compared to shallow water theory.

2.1 Equations of Motion

This section begins with the fundamental equations of motion (Section 2.1.1), followed by a review of the Boussinesq approximation (Section 2.1.2) and the f-plane and β-plane approximations (Section 2.1.3). Based on the study's focus, these equations are further simplified into 2D representations, presented in Section 2.1.4.

2.1.1 Primitive equations of the ocean

The primitive equations of the ocean are a set of nonlinear partial differential equations, derived from the Navier-Stokes equations assuming background hydrostatic balance and accounting for the effects of rotation, stratification, and external forces. The equations are derived from the continuity equation, conservation of momentum and conservation of internal energy.

The continuity equation represents the conservation of mass, stating that the rate of change of mass per unit volume of a fluid parcel is equal to the rate at which mass is flowing into or out of that fluid parcel. Mathematically this can be written as

$$\frac{\partial \varrho}{\partial t} + \boldsymbol{\nabla} \cdot (\varrho \boldsymbol{u}) = 0 \, . \tag{2.1}$$

where ϱ is the water density, $\boldsymbol{u} \equiv (u, v, w)$ is the velocity of the fluid, and $\boldsymbol{\nabla} \equiv (\frac{\partial}{\partial x}, \frac{\partial}{\partial y}, \frac{\partial}{\partial z})$ is the gradient operator here written in Cartesian co-ordinates. With the definition of the material derivative, $\mathrm{D}(\,)/\mathrm{D}t = \partial(\,)/\partial t + \boldsymbol{u} \cdot \nabla(\,)$, the continuity equation can be written as

$$\frac{\mathrm{D}\varrho}{\mathrm{D}t} = -\varrho \boldsymbol{\nabla} \cdot \boldsymbol{u} \, . \tag{2.2}$$

For the ocean, we assume the fluid to be incompressible, so that $\mathrm{D}\varrho/\mathrm{D}t = 0$ if the advection and diffusion of heat and salinity are ignored as well. Thus, from (2.2) we have

$$\boldsymbol{\nabla} \cdot \boldsymbol{u} = 0 \, . \tag{2.3}$$

The conservation of momentum states that the rate of change of momentum per unit volume of a fluid parcel is equal to the sum of the forces acting on it. Here, only the forces relevant for the dynamics in the ocean will be considered, the most significant being buoyancy, pressure gradient, and Coriolis forces, though forces due to viscous stress will also be considered. The equation for the conservation of momentum can thus be written as:

$$\varrho \frac{\mathrm{D}\boldsymbol{u}}{\mathrm{D}t} = -\nabla P + \boldsymbol{g}\varrho - (2\boldsymbol{\Omega}) \times (\varrho \boldsymbol{u}) + \mu \nabla^2 \boldsymbol{u} \, , \tag{2.4}$$

where P is pressure, $\boldsymbol{g} = -g\hat{z}$ where g is the gravitational constant and $\hat{z}$ is the vertical direction, $\boldsymbol{\Omega}$ is the angular velocity of the Earth's rotation, $\nabla^2 = \nabla \cdot \nabla$ is the Laplacian operator, and μ is the molecular viscosity. The first term on the right hand side represents the pressure gradient force, the second term is the gravitational force, the third term is the Coriolis force caused by the Earth's rotation, which plays an important role for the fluid motions that have a long time-scale compared to the Earth's rotational period. The viscous

damping force is added to the last term on the right hand side. Though it is generally negligible for large-scale motions in the ocean such as internal waves, numerical simulations often include them to damp numerical noise.

In (2.4), it is typical to separate the (total) density and pressure into background and fluctuation parts: $\varrho = \bar{\rho}(z) + \rho(z,t)$ and $P = \bar{p}(z) + p(z,t)$, where $\bar{\rho}$ and $\bar{p}$ respectively denote background density and pressure in a hydrostatic fluid, and ρ and p denote fluctuation density and pressure. In a stationary fluid, the conservation of momentum equation (2.4) implies that the pressure and density are constant at each horizontal level and vary vertically according to

$$\frac{\mathrm{d}\bar{p}}{\mathrm{d}z} = -g\bar{\rho} \, . \tag{2.5}$$

which is the statement of background hydrostatic balance. Since the ocean is a stratified fluid with density increasing with depth, we can define the buoyancy frequency (also known as Brunt–Väisälä frequency) as

$$N(z) = \sqrt{-\frac{g}{\rho_0}\frac{\mathrm{d}\bar{\rho}}{\mathrm{d}z}} \, , \tag{2.6}$$

where ρ_0 is the characteristic density of the fluid. If the density increases linearly with depth, N is constant and the fluid is said to be uniformly stratified. The real ocean is non-uniformly stratified which we will show is necessary for the internal tide to excite superharmonics.

The internal energy equation generally describes the advection and diffusion of heat and salinity in the ocean. Using the linearized equation of state for sea water to cast this equation in terms of (total) density gives

$$\frac{D\varrho}{Dt} = \kappa\nabla^2\varrho \, , \tag{2.7}$$

in which κ is the diffusivity. Writing density in terms of background and fluctuation parts gives a term, $d^2\bar{\rho}/dz^2$, from the Laplacian operator on the right hand side of (2.7), which is negligible in comparison to the Laplacian acting on fluctuation density. Thus, by defining buoyancy, $b \equiv -g\rho/\rho_0$, we can write the equation of internal energy conservation as

$$\frac{\mathrm{D}b}{\mathrm{D}t} = -N^2 w + \kappa\nabla^2 b \, . \tag{2.8}$$

In the momentum equations, the last diffusive term in (2.8) is negligible in the ocean but is included in simulations for numerical stability.

In the above we have worked with density. But at great depths in the ocean, one should use the potential density, which accounts for the influence of pressure, given by

$$\varrho_{\text{pot}} = \varrho + \varrho_0 \frac{z}{H_\rho} \,, \tag{2.9}$$

in which ϱ_0 is the reference density (at surface) and $H_\rho = 229$km is the density scale height. In what follows, we continue to use the term "density", but it is understood that we are referencing to the potential density.

2.1.2 Boussinesq approximation

The Boussinesq approximation can be invoked if the density varies only slightly over the depth of a stratified fluid. This is a good approximation for the ocean whose density typically varies by only a few percent from top to bottom. The Boussinesq approximation states that the density can be treated as a constant characteristic density, ρ_0, in all terms of the primitive equations except for the buoyancy term. This simplifies the equations of motion for the fluid while still capturing the important effects of the buoyancy force. By invoking the Boussinesq approximation and using (2.5), the momentum conservation equation (2.4) can be written explicitly in 3D Cartesian co-ordinates as

$$\frac{\mathrm{D}u}{\mathrm{D}t} - fv = -\frac{1}{\rho_0}\frac{\partial p}{\partial x} + \nu\nabla^2 u, \tag{2.10}$$

$$\frac{\mathrm{D}v}{\mathrm{D}t} + fu = -\frac{1}{\rho_0}\frac{\partial p}{\partial y} + \nu\nabla^2 v, \tag{2.11}$$

$$\frac{\mathrm{D}w}{\mathrm{D}t} = -\frac{1}{\rho_0}\frac{\partial p}{\partial z} + b + \nu\nabla^2 w, \tag{2.12}$$

where $\nu \equiv \mu/\rho_0$ is the kinematic viscosity, and f is the Coriolis parameter appearing as a consequence of approximating the Coriolis force in (2.4) onto a spherical shell, as will be discussed in the following subsection.

2.1.3 f-plane and β-plane approximation

The Coriolis parameter f in the momentum equations (2.10) and (2.11) is generally given by

$$f = 2\Omega_e \sin\theta \tag{2.13}$$

in which Ω_e is the angular velocity of Earth's rotation and θ is the latitude. While f varies with latitude, we can treat it as a constant if we are considering motion that does not deviate too far north or south about a fixed latitude, θ_0. Then we use the f-plane approximation where $f \approx f_0 \equiv 2\Omega_e \sin\theta_0$ is treated as a constant in the momentum equations.

For motion that extends more widely about a fixed latitude, we use the β-plane approximation. In terms of a Cartesian coordinate with x going from west to east and y going from south to north, a linear approximation of f in (2.13) using the Taylor expansion about $\theta = \theta_0$ gives:

$$f \approx 2\Omega_e \sin\theta_0 + 2\Omega_e(\cos\theta_0)(\theta - \theta_0) \tag{2.14}$$

$$\approx 2\Omega_e \sin\theta_0 + 2\Omega_e(\cos\theta_0)(y/R_e) \tag{2.15}$$

where y is the (north-south) distance that the fluid deviates from the fixed latitude θ_0 and R_e is the Earth's radius. Defining $\beta \equiv 2\Omega_e \cos\theta_0/R_e$, we can write

$$f \approx f_0 + \beta y \ , \tag{2.16}$$

which is the Coriolis parameter in the β-plane approximation.

To adapt the β-plane approximation for our numerical simulations of the internal tide that propagates south-west of Hawaii, we define a new coordinate system, as illustrated in Figure 1.1. The along-wave propagation direction and the spanwise direction define a right-handed coordinate system with the x-axis oriented clockwise 30° from the south and the y-axis oriented clockwise 30° from the east. Hence, the x-direction (and u for the motion) refers to the along-wave direction and the y-direction (and v) refers to the spanwise direction.

Consequently, the β-plane approximation in (2.16) becomes

$$f \approx f_0 - \beta_x x, \tag{2.17}$$

where $x = 0$ at the latitude of $\theta_0 = 18.39°$ is the location of the Farfield site located south-west of Hawaii, $f_0 = 2\Omega_e \sin\theta_0 \simeq 4.60 \times 10^{-5}\mathrm{s}^{-1}$, $\beta = 2\Omega_e \cos\theta_0/R_e \simeq 2.17 \times 10^{-11}(\mathrm{m\,s})^{-1}$, and thus $\beta_x = \beta\cos 30° \simeq 1.88 \times 10^{-11}(\mathrm{m\,s})^{-1}$ is the β parameter in the new coordinate system. The minus sign in front of β_x in (2.17) indicates that f decreases as x increases equatorward.

2.1.4 2D approximation

To simplify the problem further, as appropriate for some aspects of this study, we consider the motion of inviscid, non-diffusive, incompressible Boussinesq fluid on the β-plane in a horizontally periodic channel bounded above and below by free-slip boundary conditions. The motion is assumed to be two dimensional, with fields varying in the x and z directions. Motions may occur in the y direction as well as in x and z, but the fields have no y dependence. The 2D momentum equations are

$$\frac{\mathrm{D}u}{\mathrm{D}t} - fv = -\frac{1}{\rho_0}\frac{\partial p}{\partial x}\,, \tag{2.18}$$

$$\frac{\mathrm{D}v}{\mathrm{D}t} + fu = 0\,, \tag{2.19}$$

$$\frac{\mathrm{D}w}{\mathrm{D}t} = -\frac{1}{\rho_0}\frac{\partial p}{\partial z} + b\,, \tag{2.20}$$

where $\frac{\mathrm{D}}{\mathrm{D}t} = \frac{\partial}{\partial t} + u\frac{\partial}{\partial x} + w\frac{\partial}{\partial z}$ is the material derivative and v is the spanwise velocity.

From internal energy conservation (2.8), by neglecting diffusion, we have

$$\frac{\mathrm{D}b}{\mathrm{D}t} = -N^2 w\,. \tag{2.21}$$

The spanwise (y-component of) vorticity is defined as $\zeta \equiv \partial_z u - \partial_x w$ where the subscripts z and x denote the corresponding partial derivatives. Taking the curl of the momentum

equations in the x- and z- directions gives the time evolution of spanwise vorticity:

$$\frac{\mathrm{D}\zeta}{\mathrm{D}t} = -\frac{\partial b}{\partial x} + f\frac{\partial v}{\partial z}\,. \tag{2.22}$$

For a 2D incompressible fluid, we may define the streamfunction, ψ, such that the x- and z-velocities are

$$u = -\frac{\partial \psi}{\partial z},\ w = \frac{\partial \psi}{\partial x}. \tag{2.23}$$

From these, and the definition of ζ, it follows that

$$\zeta = -\frac{\partial^2 \psi}{\partial x^2} - \frac{\partial^2 \psi}{\partial z^2}\,. \tag{2.24}$$

By manipulating (2.3), (2.18), and (2.21), the equations can be written as a linear operator (denoted as $\mathcal{L}$) acting on the streamfunction ψ, which is forced by nonlinear terms (Baker and Sutherland, 2020):

$$\mathcal{L}\psi = \boldsymbol{\nabla}\cdot\boldsymbol{F}\,, \tag{2.25}$$

where $\mathcal{L} \equiv \partial_{tt}\nabla^2 + N^2\partial_{xx} + f^2\partial_{zz}$ and $\boldsymbol{F} \equiv \partial_t(\boldsymbol{u}\zeta) - \partial_x(\boldsymbol{u}b) + f\partial_z(\boldsymbol{u}v)$, in which the subscripts, t, x and z, denote the corresponding partial derivatives, $\boldsymbol{u} = (u, w)$, and $\nabla = (\partial_x, \partial_z)$. This equation forms the starting point for the theory of superharmonic excitation by internal tides, as discussed in Section 2.3.

2.2 Stratification

In this section, the observed stratification profiles in the Hawaiian Ocean (Section 2.2.1) and the South China Sea (Section 2.2.2) are examined, and the analytic profiles are approximated for use in numerical simulations. We use observations of potential density profiles at two locations in the ocean to derive semi-empirical formulae for $N(z)$ to be used in this study.

2.2.1 Observed stratification southwest of Hawaii

Internal tides generated by the submarine ridges near Hawaii were well-observed at the generation site and far to the southwest. At the Farfield site (see Figure 1.1), dominant mode-1

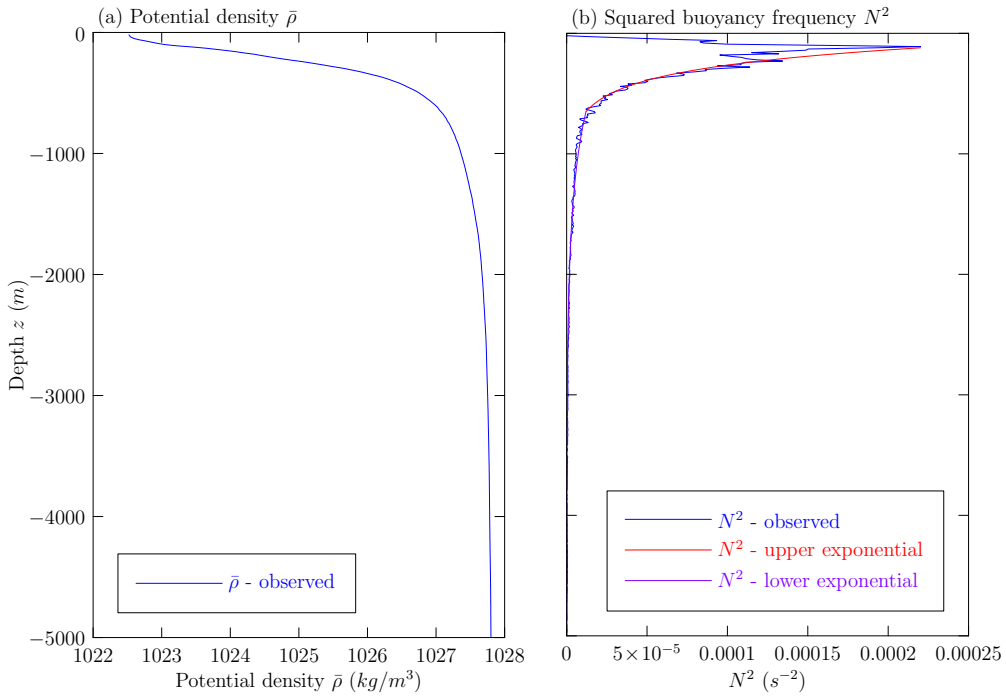

Figure 2.1: (a) Potential density obtained from the density and salinity profiles measured during UTC Nov 26th - 28th 2010, at the location of latitude 17.61°N and longitude 168.51°W (location shown in Figure 1.2). (b) Comparison of the squared buoyancy frequency (observed N^2 profile) calculated directly from the potential density shown in (a) and the piecewise N^2 profile used in the numerical simulations with upper and lower parts shown separately. (Unpublished data provided by Shaun Johnston, Scripps Institution of Oceanography)

internal tides were observed to propagate southwest towards the equator (Rainville and Pinkel, 2006). This inspires one of the interests of this study on the behaviour of internal tides travelling from a latitude where $|f| > 0$ towards the equator where $f = 0$.

The observed mean potential density profiles and corresponding squared buoyancy frequency are taken from the "EXperiment on Internal Tide Scattering" (EXITS) performed about 1000km southwest of Hawaii (unpublished data provided by Shaun Johnston, Scripps Institution of Oceanography). From one of the locations (17.61°N, 168.51°W) on the north (Hawaii-facing side) of the Line Ridge, we constructed the background stratification profile for the numerical simulations in the ocean near Hawaii. The observation location is shown in Figure 1.2 and the profiles are plotted in Figure 2.1. The dataset contains the potential density profile (Figure 2.1a) obtained from the measured pressure, temperature and salinity profiles. From this we calculate the squared buoyancy frequency N^2 according to (2.6) in which $\bar{\rho}$ is the potential density. This is plotted in Figure 2.1b. The jagged appearance of the

Parameters	Values
z_0	-120 m
z_*	-650 m
N_0	0.0206 s^{-1}
N_*	0.0038 s^{-1}
σ_1	182 m
σ_2	685 m

Table 2.1: Values for the parameters that give the best-fit piecewise exponential profile for N^2 in the Hawaiian Ocean

N^2 profile is the result of taking derivatives of coarse, discrete data. To obtain a smoother N^2 profile to be used in our simulations, we assume that N^2 can be represented by a piecewise exponential function:

$$N^2(z) = \begin{cases} N_0^2 e^{(z-z_0)/\sigma_1} & z_* \leq z \leq 0, \\ N_*^2 e^{(z-z_*)/\sigma_2} & -H \leq z < z_*, \end{cases} \tag{2.26}$$

where $N^2(z_0) = N_0^2$ and $N^2(z_*) = N_0^2 e^{(z_*-z_0)/\sigma_1} = N_*^2$, such that the two exponential functions meet at $z = z_*$. Here $z_0 \approx -100$m represents the depth of the surface-mixed layer and we set $z_* = -650$m. We find σ_1 and σ_2 that best fit the observations. The comparison of the observed N^2 and our piecewise exponential N^2 profiles with the parameters given in Table 2.1 is plotted in Figure 2.1b. We do not consider a surface-mixed layer for stratification in this study as it was demonstrated in Sutherland and Dhaliwal (2022) that the existence of a surface-mixed layer has little effect on the vertical structure of low-mode internal waves and the superharmonics they generate.

2.2.2 Observed stratification in the South China Sea

It is well-documented that solitary waves form during the evolution of westward propagating internal tides generated at Heng Chun Ridge and Lan Yu Ridge in the South China Sea (e.g. Farmer et al., 2009; Li et al., 2009). This inspires our interest in investigating the formation of solitary wave trains westward of this location.

The observation data are taken from two ocean measurements from Farmer et al. (2009)

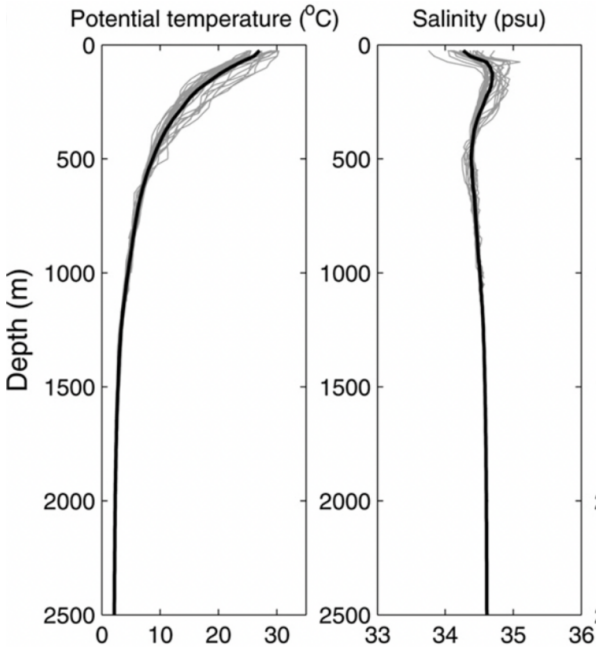

Figure 2.2: Temperature (left panel) and salinity (right panel) profiles from CTD measurements (Farmer et al., 2009) are shown in grey and the mean profiles are in black.

and Johnston et al. (2013). The first dataset measured the full-depth stratification from 5 deployments around 21°N and 119°E during 2005 and 2007, which is used as primary data to approximate the analytic profile of stratification in the numerical simulations. The second dataset only measured the stratification around the top 300 meters of the ocean at 20.71°N and 120.45°E during UTC June 14th to July 1st 2011 (data provided by Johnston et al., 2013). This is used to validate the structure of our empirically fit stratification profile near the surface.

From the mean profiles of potential temperature and salinity in Figure 2.2, Farmer et al. (2009) derived the potential density from which the buoyancy frequency profile was constructed. In the case of the South China Sea, we construct the analytic profile of N^2 also based on the piecewise-exponential function defined in (2.26), which gives a much better match to the observation than a single exponential function. Since we only have the data of potential density and the data are so noisy that they do not give a smooth derivative ($d\bar{\rho}/dz$) for the calculation of N^2, the plan to fit N^2 to observations is to integrate the two exponential

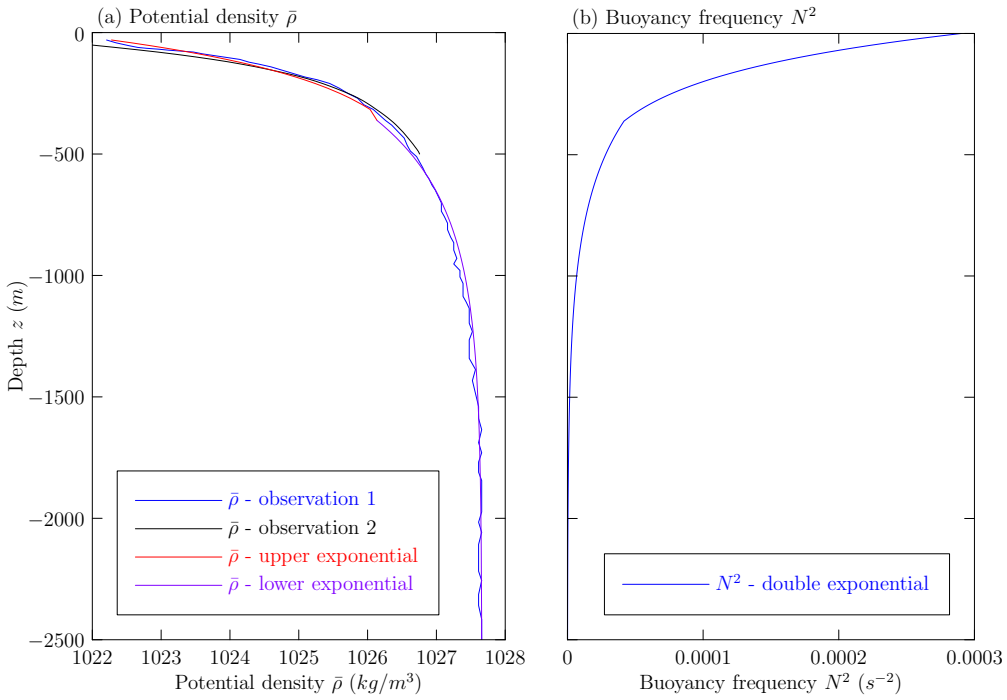

Figure 2.3: (a) Comparison of the observed potential density profile to our approximation (observation 1 from Farmer et al. (2009) and observation 2 from Johnston et al. (2013)). (b) A piecewise exponential function of squared buoyancy frequency obtained based on our approximation to the actual potential density profile.

functions defined in (2.26) to find the corresponding analytic profile of potential density:

$$\bar{\rho}(z) = \begin{cases} -\frac{\rho_0 N_0^2 \sigma_1}{g}\left[e^{-z_0/\sigma_1}\left(e^{z/\sigma_1} - e^{z_*/\sigma_1}\right)\right] + \rho_* & z_* \le z \le 0, \\ -\frac{\rho_0 N_0^2 \sigma_2}{g}\left\{e^{-(z_*/\sigma_2)-((z_0+z_*)/\sigma_1)}\left[e^{z/\sigma_2} - e^{-H/\sigma_2}\right]\right\} + \rho_b & -H \le z < z_*, \end{cases} \tag{2.27}$$

where ρ_0 is the characteristic potential density, $\bar{\rho}(z_*) = \rho_*$, and $\bar{\rho}(-H) = \rho_b$. Then we use this analytic potential density profile to match the observed potential density by finding the best-fit σ_1 and σ_2. Putting these values in (2.26), we obtain the analytic N^2 profile for the simulations. The parameters that give the best-fit result are listed in Table 2.2. The comparison of our analytic approximation to the observed potential density profile and the corresponding buoyancy frequency profile is shown in Figure 2.3.

Parameters	Values
ρ_*	1026.14 kg m^{-3}
ρ_b	1027.66 kg m^{-3}
z_0	-30.5 m
z_*	-362 m
N_0	0.0157 s^{-1}
N_*	0.0065 s^{-1}
σ_1	186 m
σ_2	351 m

Table 2.2: Values for the parameters that give the best-fit piecewise exponential profile for N^2 in the South China Sea.

2.3 Superharmonic cascade theory

This subsection introduces the theory for the superharmonic excitation of internal modes by the internal tide and the superharmonic cascade that follows. The theory employs weakly nonlinear theory and the long wave approximation. The predictions related to this study are then summarized.

2.3.1 Weakly nonlinear theory

We describe the initial structure of a small-amplitude internal tide (which we refer to as the "parent wave") with a streamfunction. With a prescribed horizontal wavenumber, k, and maximum vertical displacement amplitude, A_0, the streamfunction giving the initial structure of the parent wave is

$$\psi^{(1)}(x,z,t) = \frac{1}{2}\frac{\omega d}{k}\alpha a_1(T)\hat{\psi}_1(z)e^{\mathrm{i}(kx-\omega t)} + c.c., \tag{2.28}$$

where *c.c.* is the complex conjugate, ω is the frequency of the parent wave, d is the characteristic depth of the near-surface stratification (e.g. $d = \sigma_1$), $\alpha \equiv A_0/d$ is the non-dimensional initial amplitude of the parent wave, $a_1(T)$ represents the slow time, T, of the evolution of the amplitude, to be determined later, and $\hat{\psi}_1(z)$ gives the vertical structure, normalized to have a maximum 1. Explicitly, $\hat{\psi}_1(z)$ is determined by solving the eigenvalue problem by

substituting (2.28) into $\mathcal{L}\psi^{(1)}$=0 in (2.25):

$$\hat{\psi}_1'' + k^2 \frac{N^2 - \omega^2}{\omega^2 - f^2} \hat{\psi}_1 = 0, \quad \hat{\psi}_1(-H) = \hat{\psi}_1(0) = 0, \tag{2.29}$$

where $\hat{\psi}_1''$ denotes the second-order derivative of $\hat{\psi}_1$. For given k, the eigenvalue corresponding to the eigenfunction solution, $\hat{\psi}_1(z)$, is the frequency ω. Eq.(2.29) is solved numerically by a Galerkin method (Sutherland, 2016). We only consider mode-1 internal waves and their superharmonics for which $\hat{\psi}(z) > 0$ for $-H < z < 0$.

As studied theoretically by Baker and Sutherland (2020), the parent wave self-interacts during its propagation: the nonlinear terms on the right hand side of (2.25) result in the excitation of a superharmonic vertical mode-1 wave with a horizontal wavenumber $2k$. The parent wave and its $2k$-superharmonic can then interact and create higher superharmonics with integer multiples ($3k$, $4k$, etc.) of the wavenumber of the parent wave as well as modifying the parent wave itself. The amplitude modulation of the parent wave is given by the nondimensional function $a_1(T)$ in (2.28) where $T = \epsilon t$ is a slow timescale with $\epsilon \ll 1$, describing the slow time variation of the parent wave due to interactions with the $2k$-superharmonic.

The nondimensional slow time evolution parameter ϵ is defined as the difference between the square of the forcing frequency 2ω of the $2k$-superharmonic and the square of the natural frequency ω_2 of a vertical mode-1 internal tide with wavenumber $2k$ (Baker and Sutherland, 2020):

$$\epsilon \equiv \frac{(2\omega)^2 - \omega_2^2}{(2\omega)^2}. \tag{2.30}$$

The frequencies 2ω and ω_2 are not necessarily equal: their mismatch depends on k and the Coriolis parameter (Sutherland and Dhaliwal, 2022), as is shown in Figure 2.4. Therefore, ϵ measures the degree of the off-resonance between the forcing of the $2k$-superharmonic by the parent wave and the natural frequency of this superharmonic. As $|f|$ goes to zero (for the waves approaching the equator), ϵ goes to zero, indicating that the superharmonic forcing is in near perfect resonance.

The $2k$ and higher superharmonics likewise can be represented by the streamfunction

$$\psi^{(n)}(x, z, t) = \frac{1}{2} \frac{\omega d}{k} \alpha a_n(T) \hat{\psi}_n(z) e^{in(kx - \omega t)} + c.c., \quad n = 1, 2, 3 \ldots, \tag{2.31}$$

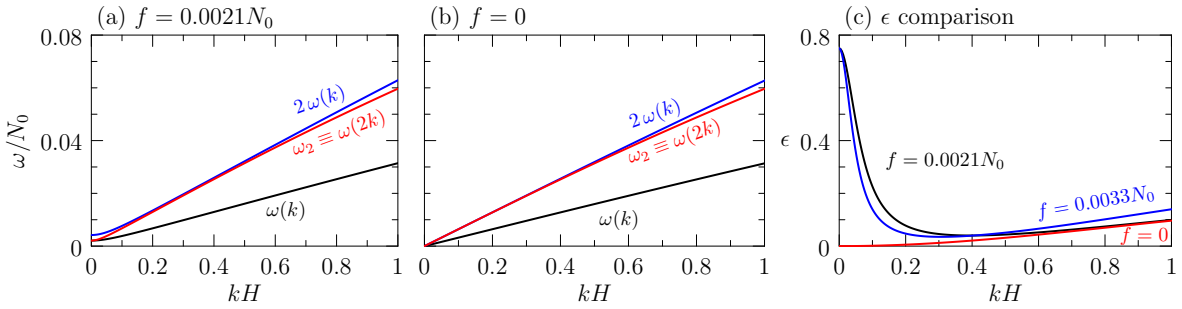

Figure 2.4: Dispersion relations for the mode-1 wave in the stratification of southwest Hawaii approximated by the piece-wise exponential function described in Section 2.2.1, with (*a*) $f = 0.00206N_0$ (based on the latitude of Farfield site) and (*b*) $f = 0$ (equator). And (*c*) The comparison of ϵ with these two Coriolis parameters, superimposed by ϵ for the wave in the South China Sea with the piecewise-exponential stratification described in Section 2.2.2 and $f = 0.0033N_0$ based on the latitude of the west propagating waves in the South China Sea.

in which $n = 1$ for the parent wave and $n = 2, 3, ...$ for the superharmonics. Likewise, the vertical structure $\hat{\psi}_n(z)$ is given by the solution to the eigenvalue problem:

$$\hat{\psi}_n'' + (nk)^2 \frac{N^2 - \omega_n^2}{\omega_n^2 - f^2}\hat{\psi}_n = 0, \quad \hat{\psi}_n(-H) = \hat{\psi}_n(0) = 0, \quad n = 1, 2, 3 \ldots , \tag{2.32}$$

where ω_n is the natural frequency of a vertical mode-1 wave with wavenumber nk and we define $\omega \equiv \omega_1$. Therefore, the streamfunction that characterizes the waves including the parent wave and its superharmonics in the domain is given by the superposition as

$$\psi(x, z, t) \approx \sum_{n=1}^{\infty} \psi^{(n)}(x, z, t), \quad n = 1, 2, 3 \ldots . \tag{2.33}$$

Given the streamfunction for the parent wave and its superharmonics, expressions for other fields can be found from the polarization relations, as listed in Table 2.3.

2.3.2 Long wave approximation

As internal tides generally have long wavelengths compared to ocean depth, for sufficiently small n, we can approximate $\hat{\psi}_n \simeq \bar{\psi}$ independent of n. The vertical structure function

Field	Polarization relation
ψ	$a_n\hat{\psi}_n$
u	$-a_n\hat{\psi}_n'$
v	$i\frac{f}{n\omega}a_n\hat{\psi}_n'$
w	$inka_n\hat{\psi}_n$
b	$N^2\frac{k}{\omega}a_n\hat{\psi}_n$
ζ	$\frac{k^2}{\omega^2}\frac{N^2-f^2}{\omega_n^2-f^2}\omega_n^2 a_n\hat{\psi}_n$

Table 2.3: Expressions for the polarization relations. The actual fields are obtained by multiplying by $\frac{1}{2}\alpha\frac{\omega d}{k}e^{i(kx-\omega t)}$ and adding the complex conjugate. Primes on $\hat{\psi}_n$ denote first-order derivative with respect to z.

satisfies a different dispersion depending upon the value of f (Sutherland and Yassin, 2022):

$$\bar{\psi}'' = \begin{cases} -(1/c^2)N^2\bar{\psi} & f = 0, \\ -\kappa^2(N^2/f^2 - 1)\bar{\psi} & |f| > 0, \end{cases} \tag{2.34}$$

where $\bar{\psi}''$ represents the second derivative of $\bar{\psi}$ with respect to z, and c and κ are the eigenvalues. The corresponding dispersion relation is

$$\omega^2 \simeq \begin{cases} c^2(nk)^2 & f = 0, \\ f^2\left[1 + (nk)^2/\kappa^2\right] & |f| > 0, \end{cases} \tag{2.35}$$

For background stratification given by the piecewise exponential in (2.26) with the parameters listed in Table 2.2, the eigenvalues are $c \simeq 0.0691HN_0$ when $f = 0$ and $\kappa \simeq 0.0474H^{-1}$ when $f = 0.0033N_0$ for the parent wave with a wavenumber $k \simeq 0.125H^{-1}$

The nonlinear forcing resulting from the interaction of a pair of waves with wavenumbers mk and lk drives a wave with wavenumber nk, such that $n = l + m$ (Sutherland and Dhaliwal, 2022). According to (2.25), we can find the equation for the forcing of waves having wavenumber nk written as

$$\mathcal{L}\psi^{(n)} = \boldsymbol{\nabla}\cdot[\partial_t(\boldsymbol{u}_m\zeta_l) - \partial_x(\boldsymbol{u}_m b_l) + f\partial_z(\boldsymbol{u}_m v_l)],\ n = m + l, \tag{2.36}$$

By manipulating (2.36), Sutherland and Dhaliwal (2022) came up with a hierarchy of

equations written explicitly in terms of the amplitude functions a_n:

$$\frac{\mathrm{d}a_n}{\mathrm{d}T} - \mathrm{i}(n-1)\omega B_n a_n = -\mathrm{i}\alpha\frac{\omega}{\epsilon}\sum_{m+l=n, m\geq l} E_{ml} a_m a_l, \quad n = 1, 2, 3, \ldots, \tag{2.37}$$

in which $n \geq 1$, both m and l are non-zero integers in the sum, and $a_{-l} = a_l^\star$, the complex conjugate of a_l. $B_1 = 0$ and $B_n = \frac{2}{n(n-1)}\frac{(n\omega)^2-\omega_n^2}{(2\omega)^2-\omega_2^2}$, $n = 1, 2, 3, \ldots$ are defined here for convenience. The coupled coefficients E_{ml} are real and positive constants. The general expressions are given by Sutherland and Dhaliwal (2022) and are simplified here by the assumption of long waves (2.35):

$$E_{ml} \simeq \begin{cases} \frac{n}{2} d \left[\int_{-H}^{0} N^2 \bar{\psi}^2 \, \mathrm{d}z\right]^{-1} \left[\int_{-H}^{0} \frac{\mathrm{d}N^2}{\mathrm{d}z} \bar{\psi}^3 \, \mathrm{d}z\right], & f = 0, \\ \frac{n}{2} d \frac{1}{1+k^2/\kappa^2} \left[\int_{-H}^{0} N^2 \bar{\psi}^2 \, \mathrm{d}z\right]^{-1} \left\{\left(\frac{k^2}{\kappa^2} + \frac{n^2 ml + m^2 + l^2}{2n^2 ml}\right)\left[\int_{-H}^{0} \frac{\mathrm{d}N^2}{\mathrm{d}z} \bar{\psi}^3 \, \mathrm{d}z\right]\right\}, & |f| > 0. \end{cases} \tag{2.38}$$

If $m = l$ which makes $n = 2m$, for $f = 0$ case, we have half the value of E_{ml} for the same value of n. As demonstrated in (2.38), the dominant contribution to E_{ml} in the long wave limit comes from integrals involving dN^2/dz, which explains why the background must be non-uniformly stratified to excite superharmonics.

The most significant changes of the parameters in (2.37) occur for ϵ, which decreases rapidly as f/N_0 goes to zero, resulting in different behaviour for superharmonic excitation depending on latitude (Sutherland and Dhaliwal, 2022). This effect can be explored by the β-plane approximation which allows f to decrease to zero as waves approach the equator, which is one goal of this thesis.

2.3.3 Theory predictions

Sutherland and Dhaliwal (2022) showed that successively higher superharmonics become excited if α/ϵ is large, where α is the nondimensional amplitude given in (2.28). When $\alpha/\epsilon \ll 1$, the influence of the superharmonic on the parent wave is negligible, and thus the slow time evolution of the parent's amplitude $a_1(T) \simeq 1$ is approximately constant. Although the $2k$-superharmonic will possibly still be excited, it will just grow and decay periodically with frequency $\epsilon\omega$ and an amplitude proportional to $\alpha/\epsilon \ll 1$. The frequency $\epsilon\omega$ is called the "beat

frequency". When $\alpha/\epsilon \gtrsim 1$, the $2k$-superharmonic can grow to a relatively large amplitude such that higher superharmonics can be excited, thereby resulting in superharmonic cascade. Though realistic internal tides in the oceans have small amplitude α, the ratio α/ϵ can still be larger than 1 due to ϵ being small. This is particularly true near the equator where ϵ is very small for $f \simeq 0$ (see Figure 2.4). With small ϵ, the beat frequency $\epsilon\omega$ is small and hence the $2k$-superharmonic can remain larger for a longer time during each "beat", over which time higher superharmonics can grow to significant amplitude. By numerically solving (2.37) and (2.38), it was shown that the superposition of superharmonics in time forms a (single) solitary wave if $\alpha/\epsilon \simeq \mathcal{O}(1)$, and forms a solitary wave train if $\alpha/\epsilon \gg 1$ (Sutherland and Dhaliwal, 2022).

The property of horizontally long internal tides forming solitary waves has been previously explored through extensions of shallow-water theory (Helfrich and Melville, 2006), namely the Ostrovsky (hereafter the KdV-f) equation (Ostrovsky, 1978). Based on the the Korteweg–de Vries (KdV) equation, the KdV-f equation includes the effect of background rotation. It is a nonlinear partial differential equation for the vertical displacement of the waves. Different from the superharmonic cascade theory that focuses on energy transferring into successively smaller scales by exciting higher harmonics, the KdV-f equation emphasizes the balance between nonlinear steepening and dispersion of long waves. Sutherland and Dhaliwal (2022) performed numerical comparisons between the KdV-f and the superharmonic cascade theories, showing that the superharmonic cascade model has good quantitative agreement with this widely-accepted model for shallow-water waves. That study was performed in two dimensions on the f-plane with an initial parent wave that was horizontally periodic. Here we extend their numerical work by examining the evolution of internal waves on the β-plane that are externally forced at a fixed spatial location with either a constant or temporally modulated amplitude. We further extend their work by examining three dimensional spanwise-localized internal tides that may disperse laterally.

Chapter 3

Numerical Methods

The theory for superharmonic excitation by internal tides given in Chapter 2 assumed the waves were small amplitude and horizontally periodic on the f-plane. To extend these predictions to realistic internal tides, we perform fully nonlinear numerical simulations. Three distinct numerical models are used, which model 2D horizontally periodic waves on the f-plane (Section 3.1), 2D forced waves on the β-plane (Section 3.2), and 3D streamwise-periodic spanwise-localized waves on the f-plane (Section 3.4), respectively. The 2D model in Section 3.1 is the original model that has previously been used to simulate the superharmonics excited by nonlinear interactions within internal waves (Sutherland, 2016). This model was adapted to have numerical forcing that generated vertical mode-1 waves at a fixed horizontal location and was extended to include wave evolution on the β-plane to examine the evolution of the waves as they approach the equator. The 3D model (Section 3.4) more realistically shows the lateral spreading of internal tides that emanate from the source as a spanwise-confined beam. Below, after introducing each model, we describe the methods used to analyze the results from the 2D and 3D simulations.

3.1 2D horizontally periodic waves on f-plane

3.1.1 Equations and numerical dissipation

We did not directly solve the x- and z-momentum equations (2.18) and (2.20) to get u and w because we would additionally need to solve a diagnostic equation for pressure. Instead,

making use of incompressibility for a 2D flow, the code computed the evolution of the spanwise vorticity ζ, which could be inverted to find streamfunction by (2.24). The velocity fields, u and w, were then derived using (2.23).

The time evolution of spanwise vorticity ζ, spanwise velocity v, and buoyancy b on the x-z plane are given explicitly by

$$\frac{\partial \zeta}{\partial t} = -u\frac{\partial \zeta}{\partial x} - w\frac{\partial \zeta}{\partial z} - \frac{\partial b}{\partial x} + f\frac{\partial v}{\partial z} + \nu \mathcal{D}\zeta, \tag{3.1}$$

$$\frac{\partial v}{\partial t} = -u\frac{\partial v}{\partial x} - w\frac{\partial v}{\partial z} - fu + \nu \mathcal{D}v, \tag{3.2}$$

$$\frac{\partial b}{\partial t} = -u\frac{\partial b}{\partial x} - w\frac{\partial b}{\partial z} - N^2 w + \kappa \mathcal{D}b. \tag{3.3}$$

These are extensions, respectively, of (2.22), (2.19), and (2.21) to include viscous and diffusive terms. However, the diffusion operator $\mathcal{D}$ is a Laplacian operator acting only upon horizontal Fourier components (see below) with horizontal wavenumber greater than a cut-off wavenumber, $n_c k$, where k is the prescribed horizontal wavenumber of the parent internal tide. We typically used a cut-off of $n_c = 128$. The Reynolds number, $\mathrm{Re} = H^2 N_0/\nu$, was set to 10^5 and the Prandtl number, $\mathrm{Pr} = \nu/\kappa$, was set to 1, where ν is the kinematic viscosity and κ is the diffusivity. Although these numbers are much smaller than realistic values in the oceans, they were added to the equations for the purpose of numerical stability, serving to damp numerical noise. Since diffusivity was not applied to disturbances with wavenumbers smaller than $n_c k$, the parent wave and excited superharmonics that reached significant amplitudes were effectively inviscid and non-diffusive.

3.1.2 Discretization and resolution

The fields and parameters in the code were all non-dimensional. All the length-related units were scaled by the ocean depth H and all time-related units were set by the characteristic buoyancy frequency N_0. The code initialized the waves in a rectangular domain with horizontally periodic boundary conditions and free-slip conditions at the top and bottom boundaries. The domain was discretized on an evenly spaced grid in the z-direction and in terms of their horizontal Fourier components in the x-direction (spectral representation). In horizontal Fourier space, partial derivatives with respect to x were replaced by algebraic expressions,

e.g.:

$$\frac{\partial}{\partial x} \rightarrow \mathrm{i}k_n, \tag{3.4}$$

where k_n denotes the n-th horizontal wavenumber in the domain, i.e. $k_n = nK_0$, where $K_0 = 2\pi/L$ and L is the length of the domain. The horizontal Fourier decomposition was rapidly converted into real space using fast Fourier transforms. In the vertical, for partial derivatives with respect to z, we used a centered, second-order finite-difference scheme.

The resolution typically consisted of 257 vertical levels and 1024 horizontal Fourier components, corresponding to 257×2049 grid points in real space. Various resolutions were tested and it was found that doubling the resolution from 257×2049 in both directions did not quantitatively influence the results.

3.1.3 Initialization

The background stratification was set by the piecewise exponentials described in Section 2.2.1 and 2.2.2. The model initialized a horizontally periodic parent wave with a prescribed horizontal wavenumber k and vertical displacement amplitude A_0 in the domain at t=0. The streamfunction characterizing the parent wave at $t = 0$ was given by

$$\psi(x, z, 0) = \frac{1}{2}\frac{\omega}{k} A_0 \hat{\psi}(z) e^{\mathrm{i}kx} + c.c. = \frac{\omega}{k} A_0 \hat{\psi}(z) \cos(kx). \tag{3.5}$$

Using the polarization relations (Table 2.3), the other initial basic state fields, u, w, v, b, and ζ, were prescribed.

3.1.4 Time step

For time-stepping, based on the numerical stability conditions, an Euler forward scheme was used for diffusive terms and a leapfrog scheme was employed to advance in time the non-diffusive terms:

$$\zeta(x, z, t + \Delta t) = \zeta(x, z, t - \Delta t) + 2\Delta t \dot{\zeta}, \tag{3.6}$$

where $\dot{\zeta}$ is the time derivative of ζ given by right-hand side of (3.1) without the diffusive term and Δt is the time step. Likewise, this scheme was used for the b and v fields. One loop of the leapfrog scheme involved $n_e = 20$ small time steps of $\Delta t = 0.05 N_0^{-1}$. So time was advanced by $1 \times N_0^{-1}$ after each loop. To avoid splitting errors, the last time step in each loop was obtained by averaging the fields from the leapfrog steps at $n_e \Delta t$ and the field found from taking an Euler backstep by Δt from the field at step $(n_e + 1)\Delta t$:

$$\zeta(x, z, t_{21}) = \zeta(x, z, t_{19}) + 2\Delta t \dot{\zeta}, \tag{3.7}$$

$$\zeta(x, z, t_{20}) = \frac{[\zeta(x, z, t_{18}) + 2\Delta t \dot{\zeta}] + [\zeta(x, z, t_{21}) - \Delta t \dot{\zeta}]}{2}, \tag{3.8}$$

in which the subscript of t denotes the sequence of time step in a leapfrog loop.

3.2 2D forced waves on the β-plane

The excitation of superharmonics and the formation of solitary wave trains are influenced by the Coriolis force (Sutherland and Dhaliwal, 2022) with longer wave trains developing if the Coriolis parameter is smaller (e.g. waves near the equator). To examine the smooth transition of the wave evolution as the Coriolis parameter becomes smaller, the original 2D model was extended to include rotation on the β-plane where the Coriolis force varies continuously with latitude. The β-plane approximation used in the model is given by (2.17). This allows us to improve our understanding of the evolution of internal tides, particularly for those that propagate toward the equator. This model is also used to examine the spatial evolution of waves as they propagate away from their generation site. The results can thus be compared with observations of the internal tide evolving to form a solitary wave, for example, in the South China Sea.

3.2.1 Numerical forcing

To examine the spatial evolution of waves as they propagate away from their generation site, we added numerical forcing to generate the waves in an initially stationary background. The waves were excited over the model ocean depth at a fixed horizontal location which we denoted

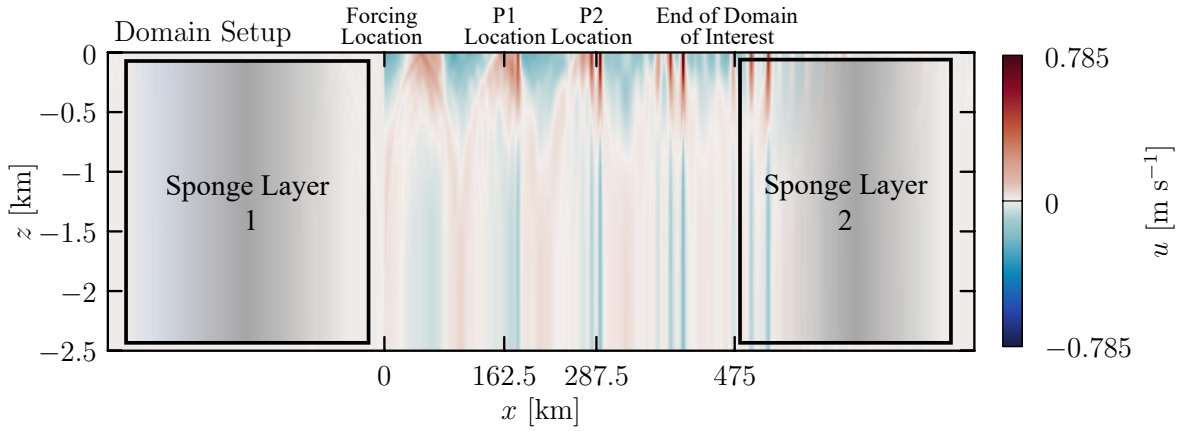

Figure 3.1: Domain setup with an example of velocity field in a simulation with temporally forced waves at $x = 0$.

by $x = 0$ (see Figure 3.1). The amplitude of forcing smoothly increased in time from zero to either a constant or modulated value in time. The modulation was intended to model the effect of the amplitude modulation of the semi-diurnal tide between spring and neap tides. With the implementation of numerical forcing in a horizontally periodic domain, we must have two sponge layers at both sides of the domain to dissipate the signals of the waves before they reached the left and right sides of the domain (see Figure 3.1). The details of these adaptations will be discussed in what follows. Any other aspects of the model not mentioned in this section are the same as described in Section 3.1.

The numerical forcing terms in the three main equations for vorticity (ζ), spanwise velocity v, and buoyancy b respectively are $\mathcal{F}_\zeta$, $\mathcal{F}_v$, and $\mathcal{F}_b$ which are added to the right-hand side of the three evolution equations, (3.1), (3.2), and (3.3). These are derived from the polarization relations (Table 2.3), and are given explicitly below

$$\mathcal{F}_\zeta = A_f(t) k \omega^2 \frac{N^2 - f^2}{\omega^2 - f^2} \hat{\psi} \sin(\omega t) \Delta(x), \tag{3.9}$$

$$\mathcal{F}_v = -A_f(t) f \frac{\omega}{k} \hat{\psi}' \cos(\omega t) \Delta(x), \tag{3.10}$$

$$\mathcal{F}_b = A_f(t) N^2 \omega \hat{\psi} \sin(\omega t) \Delta(x). \tag{3.11}$$

Here ω is the forcing frequency, which we take to correspond to that of the semi-diurnal lunar tide (M_2). $\Delta(x)$ represents the horizontal span of the forcing, which typically we apply only to the grid point where $x = 0$. The time-varying forcing amplitude of vertical displacement

is given generally by

$$A_f(t) = \{\frac{1}{2}A_{F0}[\tanh(\frac{t-t_0}{\delta_t}) + 1]\}\{1 + A_M \cos[\omega_M(t-t_1)]\}, \tag{3.12}$$

An example of the time-varying forcing amplitude A_f is plotted in Figure 3.2(a). In all 2D forced-waves simulations, t_0 and δ_t are set to $500N_0^{-1}$ and $125N_0^{-1}$, respectively. We vary the vertical displacement amplitude, A_{F0}, and its relative periodic modulation, A_M, with the modulation frequency ω_M. The hyperbolic tangent function stabilizes the code by allowing the forcing amplitude to increase smoothly from near zero to the establishment of steadily forced waves over a time $t_1 = 2t_0 = 1000N_0^{-1}$, corresponding to $\simeq 13.5$ hours for $N_0 = 0.0206\text{s}^{-1}$. The modulation is thus shifted in time by t_1 to begin at its maximum once the forcing reaches steady state. The mean forcing amplitude is A_{F0}, whereas the resulting forced waves have observed amplitude A_0, which is measured at a quarter wavelength to the right of the forcing location. This is typically double A_{F0}. The discrepancy between A_0 and A_{F0} is a result of the application of the forcing to a vertical slice at a single horizontal location. This signal is subsequently damped immediately after the forcing is applied. When presenting the results, we will refer to A_0 as the maximum forcing amplitude, since it reflects the actual amplitude of the waves generated by the forcing.

We estimated the relative modulation amplitude and frequency in (3.12) based on the Farfield observations south-west of Hawaii (Rainville and Pinkel, 2006) and the observations in the South China Sea (Johnston et al., 2013): $A_M \simeq 0.5$ or 0 for having modulation effective or not, and $\omega_M \simeq 0.000235N_0$ for $N_0 = 0.0206\text{s}^{-1}$, corresponding to $\simeq 15$ days, which is the modulation period of the semi-diurnal tide. We also varied the relative vertical displacement amplitude A_0 from $0.002H$ to $0.012H$ in the experiments of the South China Sea to examine the dependence of solitary wave trains on the amplitude of the forcing. For $H = 2500$m, this corresponds to internal tides initially having vertical displacement amplitudes between 5m and 30m.

3.2.2 Sponge layers

Since the signals of the waves excited by the numerical forcing can propagate in both left and right directions, it is necessary to have sponge layers on both sides of the domain. In the sponge layers, the diffusion operator $\mathcal{D}$ in (3.1), (3.2) and (3.3) acts on all horizontal Fourier components: $\mathcal{D} = \nu\alpha(x)\nabla^2$, where $\alpha(x)$ is the relative increase in viscosity toward the left and right of the domain. The relative viscosity was increased smoothly to have progressively higher value from within the domain at the edge of each sponge layer to the sides of the domain. For example, in the left sponge layer, $\alpha(x)$ is given explicitly by

$$\alpha(x) = \frac{1}{2}\alpha_0[\tanh(-\frac{x - x_1}{\delta_x}) + 1] \quad x < x_{\text{right}}. \tag{3.13}$$

This is plotted in Figure 3.2(b). In (3.13), $x_{\text{right}} = -20H$, $x_1 = -31H$, $\delta_x = 2.5H$, and $\alpha_0 = 6$ gives the maximum increase of the viscosity in the sponge layer. These values allows the sponge layer to cancel the wave signals effectively without destabilizing the numerical model.

3.3 Analysis methods for 2D simulations

To characterize the structure of solitary wave trains that form during the propagation of internal tides, we measured the maximum vertical displacement of isopycnals at a fixed point in the domain. The vertical displacement, ξ, is given by $\xi = -b/N^2$, in which b is buoyancy. Specifically, the measurement was taken at a depth z_{m} where the vertical structure of the streamfunction, and hence vertical displacement, was greatest ($\hat{\psi} = 1$). In the simulations of the South China Sea, this occurred where $z_{\text{m}} = -700$m. The horizontal location of the measurement was set according to ocean observations so that simulations could be compared to observations. For example, in simulations representative of the South China Sea, the measurement was taken at $x = 162.5$km and $x = 287.5$km. These correspond to the P1 and P2 observation locations (see Figure 1.4) in Farmer et al. (2009), where the ocean depth is about 2500m. An example of the vertical displacement over time at P2 is shown in Figure 3.3. From this we determined the number of waves (denoted by red diamonds) in a solitary

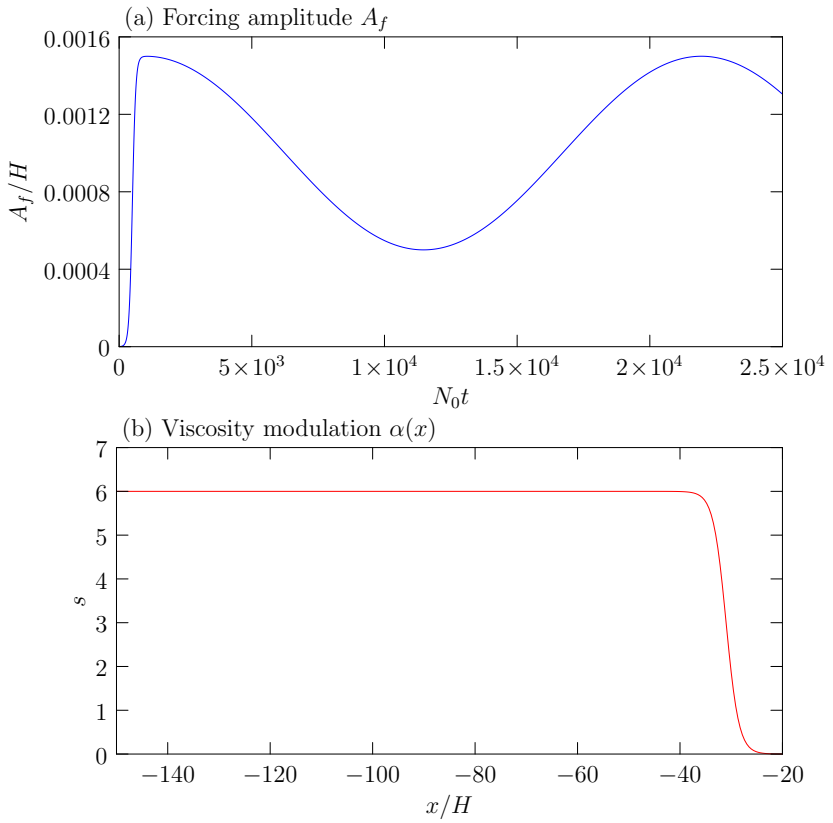

Figure 3.2: (a) Forcing amplitude over time given by (3.12) with the parameters $A_0 = 0.001H$, $t_0 = 500N_0^{-1}$, $\delta_t = 125N_0^{-1}$, $A_M = 0.5$, $\omega_M = 0.0003N_0$, and $t_1 = 1000N_0^{-1}$. (b) Viscosity modulation $\alpha(x)$ in the left sponge layer given by (3.13) with the parameters $\alpha_0 = 6$, $x_{\text{right}} = -20H$, $x_1 = -31H$, and $\delta_x = 2.5H$.

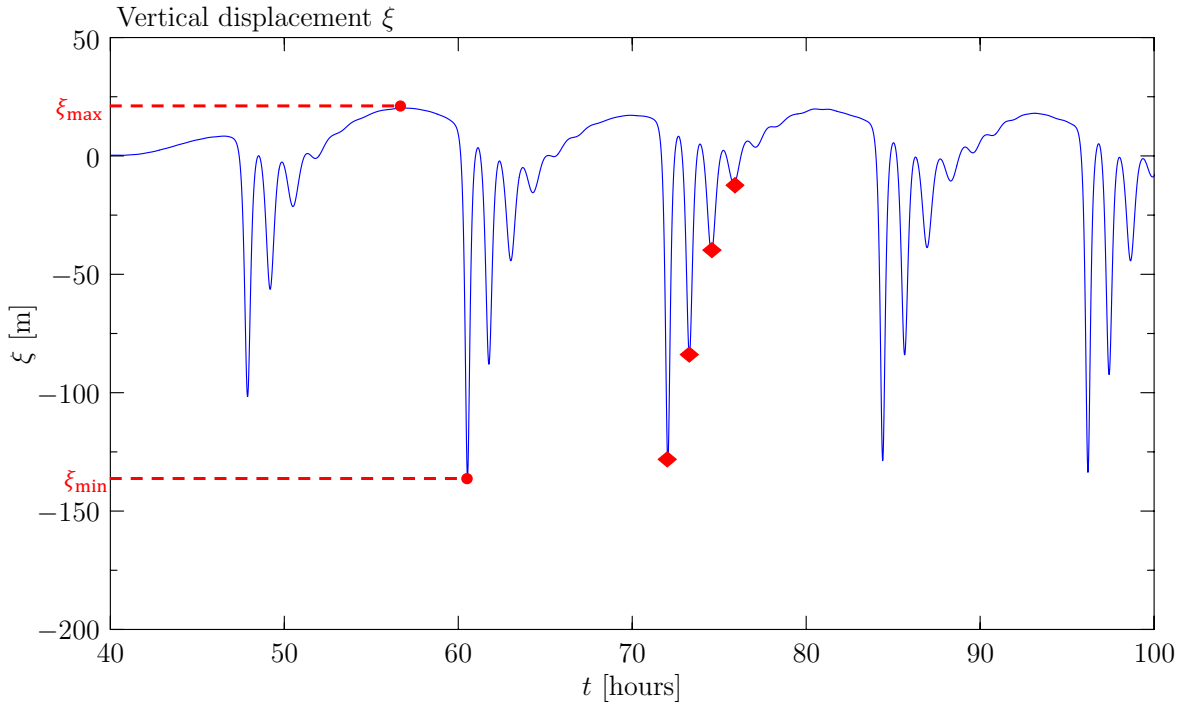

Figure 3.3: Vertical displacement ξ over time, measured at the P2 location ($x = 287.5$km and $z_m = -700$m) in the domain, from a 2D simulation of forced waves with the parameters: $A_0 = 40$m, $k \simeq 4.8 \times 10^{-5}\text{m}^{-1}$, $\omega \simeq 1.44 \times 10^{-4}\text{s}^{-1}$ and $f_0 \simeq 5.2 \times 10^{-5}\text{s}^{-1}$. The background stratification N^2 is given by the piecewise exponential (2.26) with the parameters listed in Table 2.2.

wave train as well as the minimum and maximum vertical displacements (denoted by $\xi_{\min}$ and $\xi_{\max}$).

The simulations are also used to compare the velocity associated with solitary waves. Time series of the along-wave velocity (u), as shown for example in Figure 3.4, can be compared with ocean observations. In the South China Sea, for example, we use the observation data close to the P1 location (see Figure 1.4) provided by Johnston et al. (2013), who measured the velocities in time over the top 500m of the ocean (see Section 4.4). Likewise, we use the observations from EXITS by Shaun Johnston, Scripps Institution of Oceanography.

Inspired by observations of south-westward internal tides emanating from Hawaii, we compared the simulations of internal tides on the f-plane with different fixed values of f, with simulations on the β-plane for which f varies continuously in space. The simulations on the β-plane predicted the distance from the source at which solitary waves began to form and evolved into a solitary wave train.

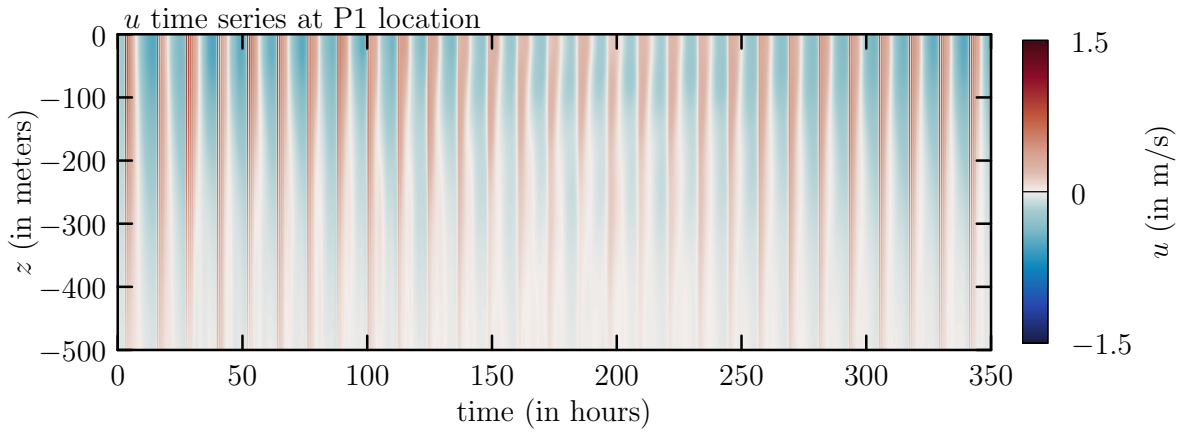

Figure 3.4: Time series of u velocity, measured at the P1 location in the domain, from a 2D simulation of forced waves with the parameters: $A_0 = 40\text{m}$, $k \simeq 4.8 \times 10^{-5}\text{m}^{-1}$, $\omega \simeq 1.44 \times 10^{-4}\text{s}^{-1}$ and $f_0 \simeq 5.2 \times 10^{-5}\text{s}^{-1}$. The background stratification N^2 is given by the piecewise exponential (2.26) with the parameters listed in Table 2.2.

3.4 3D model

The 3D model more realistically simulated the evolution of internal tides by considering the influence of waves having a finite spanwise extent leading to lateral spreading even as the waves possibly steepen to form solitary waves. Because these simulations required more memory to resolve the spanwise structure, and consequently took longer to run, we restricted this study to streamwise periodic waves on the f-plane, for which the horizontal extent of the domain could be smaller.

3.4.1 Equations

The fully nonlinear 3D simulations were achieved by numerically solving the time evolution of velocities in the x and y direction, denoted as u and v, respectively, along with the vertical displacement ξ of the isopycnals, given in terms of perturbation density, ρ, by $\xi = -\rho/(d\bar{\rho}/dz)$. The equations for horizontal momentum and internal energy, neglecting viscosity and diffu-

sion, are

$$\frac{\partial u}{\partial t} = -\frac{\partial u^2}{\partial x} - \frac{\partial vu}{\partial y} - \frac{\partial wu}{\partial z} + f_0 v - \frac{1}{\rho_0}\frac{\partial p}{\partial x}, \tag{3.14}$$

$$\frac{\partial v}{\partial t} = -\frac{\partial uv}{\partial x} - \frac{\partial v^2}{\partial y} - \frac{\partial wv}{\partial z} - f_0 u - \frac{1}{\rho_0}\frac{\partial p}{\partial y}, \tag{3.15}$$

$$\frac{\partial \xi}{\partial t} = -\frac{\partial u\xi}{\partial x} - \frac{\partial v\xi}{\partial y} - \frac{\partial w\xi}{\partial z} + w. \tag{3.16}$$

These simulations were performed on the f-plane, so f_0 is constant. The dynamic pressure, p, and vertical velocity, w, were found by the diagnostic equations:

$$\begin{aligned}\frac{1}{\rho_0}\nabla^2 p = &-\left[\frac{\partial^2\left(u^2\right)}{\partial x^2} + \frac{\partial^2\left(v^2\right)}{\partial y^2} + \frac{\partial^2\left(w^2\right)}{\partial z^2}\right] - 2\left[\frac{\partial^2(uv)}{\partial x \partial y} + \frac{\partial^2(uw)}{\partial x \partial z} + \frac{\partial^2(vw)}{\partial y \partial z}\right] \\ &+ f\frac{\partial v}{\partial x} - f\frac{\partial u}{\partial y} - N^2\frac{\partial \xi}{\partial z},\end{aligned} \tag{3.17}$$

and

$$\frac{\partial w}{\partial z} = -\frac{\partial u}{\partial x} - \frac{\partial v}{\partial y}. \tag{3.18}$$

Equation (3.17) is given by the divergence of the momentum equations, (2.10), (2.11), and (2.12). Equation (3.18) is from the incompressibility of the fluid, given by (2.3).

Equations (3.14) – (3.16) do not include Laplacian diffusion, usually used for numerical stability. Since numerical noise in the 3D model grew faster compared to the 2D models, we instead applied an exponential filter to (3.14), (3.15), and (3.16) at every time step as described in Section 3.4.3.

3.4.2 Discretization and resolutions

The 3D model used the same non-dimensionalization scheme as the 2D models: the length-related units were scaled by the ocean depth H and all time-related units were set by the characteristic buoyancy frequency N_0. The 3D model used a rectangular domain with horizontally periodic boundary conditions and free-slip upper and lower boundary conditions. A spectral representation was used for the horizontal fields, being decomposed into their Fourier components in the x and y directions. The vertical fields were decomposed into Fourier cosine

series for u and v and Fourier sine series for ξ. Explicitly, for sine vertical structure,

$$\hat{\xi}(z) = \sum_{n=1}^{n=n_z} \xi_n \sin(m_n z), \quad m_n = n(\pi/H) \quad \text{and} \quad n = 0, 1, 2, \cdots, \tag{3.19}$$

in which n_z is the number of vertical modes.

The spatial domain was of size $L_x \times L_y \times L_z$. The streamwise dimension was set by $L_x = 2\pi n_x/k_x$, where n_x and k_x were the number of wavelengths and the horizontal wavenumber in the streamwise direction, respectively. The vertical dimension was set as $L_z = H$. The spanwise dimension was specified directly as $L_y = 500H$ or $1000H$ depending on the spanwise width of the waves. Typically, 512 and 256 grid points were used in the streamwise and vertical dimensions, respectively. Depending on the spanwise width of the waves, 256 or 512 grid points were used in the spanwise direction.

3.4.3 Exponential filter

In this approach, the Fourier components with wavenumber higher than a specific cut-off wavenumber, $n_{\text{cut}}k$, were damped exponentially with increasing wavenumber (Subich et al., 2013). Taking Fourier components in the x direction as an example, a Fourier field f_n was filtered by $f_n \to \chi f_n$ for $n \geq n_{\text{cut}}$ in which

$$\chi(n) = \begin{cases} 1, & n < n_{\text{cut}}, \\ \exp\left[-e_1 \left(\frac{n-n_{\text{cut}}}{n_{\text{mx}}-n_{\text{cut}}}\right)^{e_2}\right], & n \geqslant n_{\text{cut}}. \end{cases} \tag{3.20}$$

Here e_1 is the filter strength, e_2 is the filter order, and $n_{\text{mx}} = 256$ is the total number of Fourier components in the x direction. We used the default values provided in Subich et al. (2013): $n_{\text{cut}} = 0.6n_{\text{mx}}$, $e_1 = 20$, and $e_2 = 2$. Using this filter and the provided values for the coefficients, numerical noise was damped effectively without affecting the wavenumbers with non-negligible amplitude.

3.4.4 Initialization and time-stepping

As an extension to the 2D model in Section 3.1, a parent wave with a prescribed horizontal wave number k and vertical displacement amplitude A_0 was initialized in the domain at $t = 0$. The background stratification profile was identical to the 2D model, constructed by our piecewise exponential described in Section 2.2.1 and 2.2.2. The parent wave was a plane wave in the x direction with amplitude decaying as a Gaussian in the y direction centered at $y = 0$. In particular, the vertical displacement, ξ, characterizing the parent wave at $t = 0$ was given by

$$\xi(x, y, z, 0) = \frac{1}{2} A_0 e^{-\frac{1}{2}(\frac{y}{\sigma_y})^2} \hat{\psi}(z) e^{\mathrm{i}kx} + c.c., \tag{3.21}$$

where $\hat{\psi}$ is the vertical structure of the streamfunction given by the solution of the eigenvalue problem (2.32), and σ_y is the standard deviation of the Gaussian. With the polarization relations listed in Table 2.3, we also have the u and v fields at $t = 0$ given by

$$u(x, y, z, 0) = A_0 e^{-\frac{1}{2}(\frac{y}{\sigma_y})^2} \frac{\omega}{k} \hat{\psi}'(z) e^{\mathrm{i}kx} + c.c. \tag{3.22}$$

$$v(x, y, z, 0) = \mathrm{i} A_0 e^{-\frac{1}{2}(\frac{y}{\sigma_y})^2} \frac{f_0}{k} \hat{\psi}'(z) e^{\mathrm{i}kx} + c.c., \tag{3.23}$$

in which $\hat{\psi}'$ is the first-order derivative of $\hat{\psi}$ with respect to z.

Figure 3.5 shows cross-sections of the initial streamwise velocity field (u) which has four streamwise waves in the x direction of wavelength $\lambda_x = 50H$ and spanwise width is $2\sigma_y = 40H$. The wavelength and width were estimated from satellite observations of solitary waves in the South China Sea for which $\lambda_x \simeq 125$km and $2\sigma_y \simeq 100$km.

The time scheme for the 3D model employed the same leapfrog method as used in the 2D model for the non-diffusive terms (see Section 3.1.4).

3.4.5 Analysis methods

In the 3D simulations, our primary focus was on the effects of spanwise-finite internal tides on their evolution. For example, Figure 3.6 shows vertical and horizontal cross-sections taken from the simulation shown in Figure 3.5 at time $t = 3000N_0^{-1}$ corresponding to about 53 hours with $N_0 = 0.0157\mathrm{s}^{-1}$. This shows the formation of solitary waves even while the waves

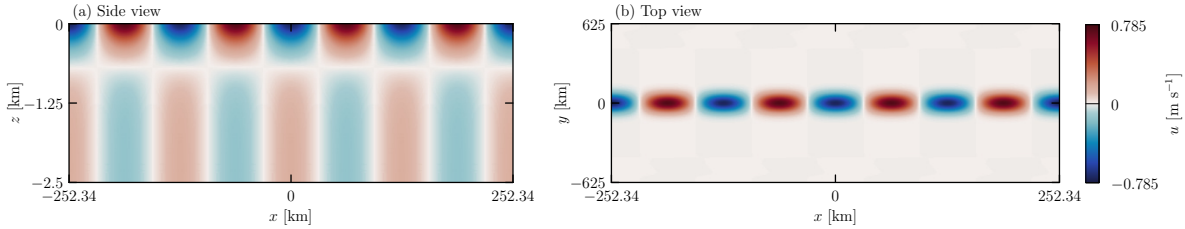

Figure 3.5: Initial stage of the streamwise velocity field $u(x, y, z, 0)$: (a) top view, on the xz-plane at $y = 0$, and side view, on the xy-plane at $z = 0$, from the simulation with the parameters: ocean depth $H = 2500$m, the initial vertical displacement amplitude $A_0 = 75$m, the horizontal wavenumber $k_0 \simeq 4.8 \times 10^{-5}\text{m}^{-1}$, the spanwise width $\sigma_y = 50$km, the wave frequency $\omega \simeq 1.47 \times 10^{-4}\text{s}^{-1}$. The background stratification N^2 is given by the piecewise exponential (2.26) with the parameters listed in Table 2.2.

spread laterally.

We began by conducting a qualitative comparison between the 2D and 3D simulations of horizontally periodic waves through the examination of the surface velocity and vertical cross-sections of horizontal velocity at $y = 0$. Next, we performed quantitative comparisons by examining the time series of maximum vertical displacement and streamwise velocity at $y = 0$. Also, we used the same method as the 2D simulations to analyze the solitary wave trains in the 3D simulations at $y = 0$ to make comparisons between the two. In the 2D-forced simulations of waves in the South China Sea, measurements were taken to correspond to the P1 and P2 locations (see Figure 3.1). Since the 3D model simulates the initialized parent wave in a horizontally periodic domain, the P1 and P2 locations were approximately associated with an evolution time, set by the time to propagate at the horizontal group velocity, c_{gx}, from the forcing location to the P1 and P2 locations. For example, with the predicted group velocity in the x direction, $c_{gx} \simeq 2.55\text{ms}^{-1}$, the waves would take $\simeq 17.7$ hours $(1000N_0^{-1})$ to reach P1 and $\simeq 41$ hours $(2320N_0^{-1})$ to reach P2 from the estimated generation site (122°E in Figure 1.4).

To examine the spanwise spreading of the waves, we determined the location in time of the wave edge, $y_{\max}(t)$, defined as where the peak surface u velocity at y is 1% of the peak u velocity at $y = 0$ and at time t. This is indicated by the black-dashed line in Figure 3.6 which plots the surface u velocity after the waves have evolved for about 53 hours $(3000N_0^{-1})$. Apart from the wave edge, the spanwise spreading of the waves also showed a surface signature which is visible in satellite images (e.g. see Figure 1.4). These bright-banded surface signatures are caused by horizontally convergent flow associated with horizontal surface current gradients

(e.g. $\partial u/\partial x$), making the water surface rougher. The minimum range of the surface current gradients to be visible by satellites is 10^{-4}–$10^{-3}\mathrm{s}^{-1}$ (Alpers, 1985). We chose the critical threshold, $(\partial u/\partial x)_c = 2 \times 10^{-4}\mathrm{s}^{-1}$, and measured the width of the surface signature where $\partial u/\partial x > (\partial u/\partial x)_c$. This value of $(\partial u/\partial x)_c$ was chosen from the typical range so that we were able to show the growth and decay of the width of the surface signature, which could be compared with satellite observations.

As the waves propagated in the x direction, their shape in the y direction bent to form an arc, which we found to be well-approximated about $y = 0$ by a parabola. We characterized this deformation by fitting at each time a parabola of the form $x = ay^2 + x_0$ to the contours where $\partial u/\partial x = 0$. These contours indicated the peaks of solitary waves between the positive and negative flows, for example, the green curve in Figure 3.6 (c). The radius of curvature, R_c, was then calculated by $R_c = 1/(2a)$. Thus a measure of the evolution of the radius of curvature in time is given by $R_c(t)$. These analysis were applied to a range of simulations with parameters appropriate for the South China Sea. The results are presented in Chapter 5.

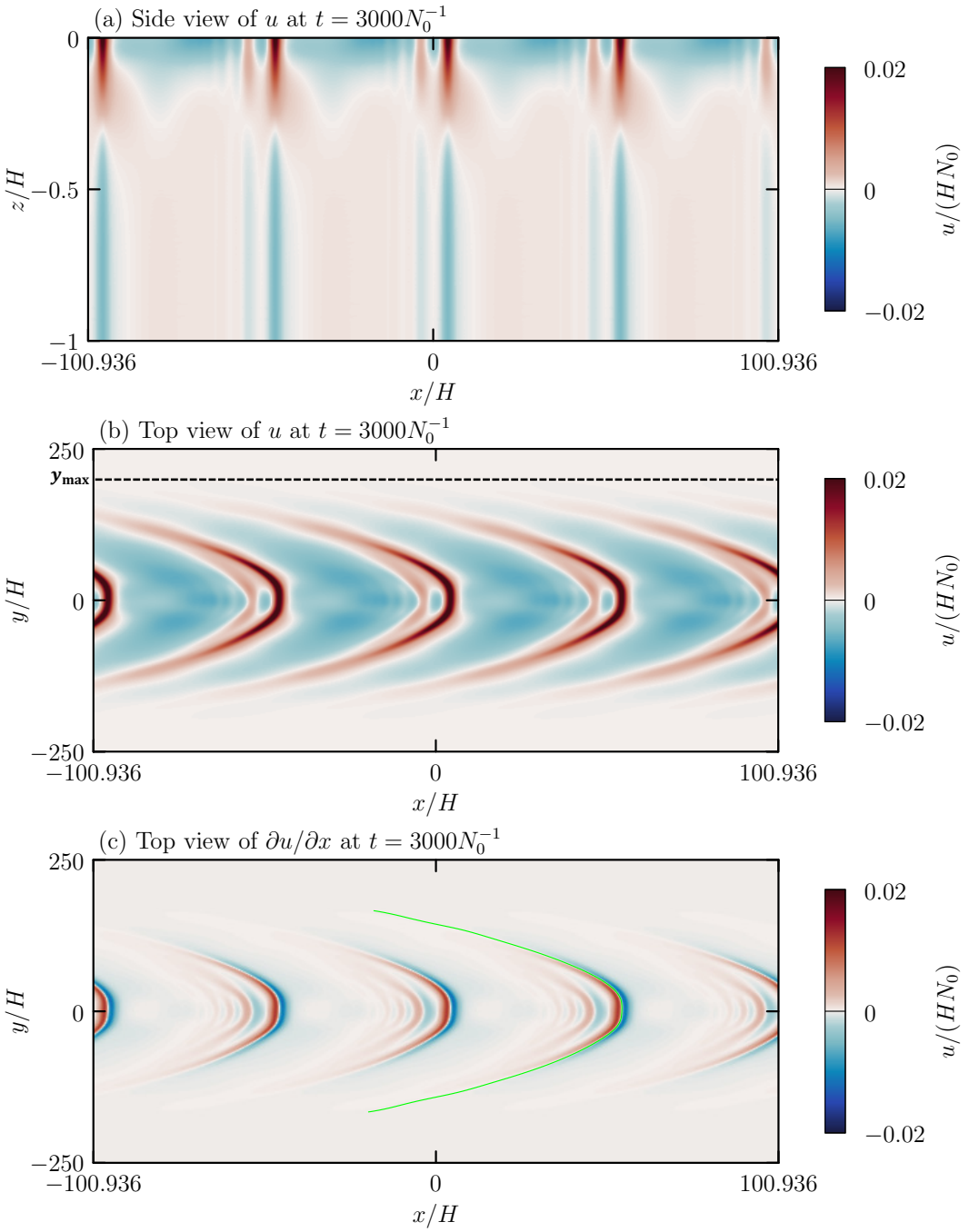

Figure 3.6: (a) side-view snapshot of the streamwise velocity, u, at $y = 0$. (b) top-view snapshot of the u field at $z = 0$ with the width edge, $y_{\max} \simeq 450$km, plotted in black-dashed line. (c) top-view snapshot of the $\partial u/\partial x$ field at $z = 0$ with the contour ($\partial u/\partial x = 0$) plotted in green. These are from the same simulation shown in Figure 3.5 but at a later time, $t = 3000N_0^{-1}$ (corresponding to $\simeq 53$ hours with $N_0 = 0.0157\text{s}^{-1}$), with the parameters: ocean depth $H = 2500$m, the initial vertical displacement amplitude $A_0 = 75$m, the horizontal wavenumber $k_0 \simeq 4.8 \times 10^{-5}\text{m}^{-1}$, the spanwise width $\sigma_y = 50$km, the wave frequency $\omega \simeq 1.47 \times 10^{-4}\text{s}^{-1}$. The background stratification N^2 is given by the piecewise exponential (2.26) with the parameters listed in Table 2.2.

Chapter 4

2D Simulation Results

In this chapter, simulations results from the 2D models are presented. Although the simulations were performed with nondimensional parameters based on depth scale, H, and time scale, N_0^{-1}, the results here are given in dimensional units relevant to observations in the South China Sea (Farmer et al., 2009; Johnston et al., 2013) and southwest of Hawaii (through the unpublished EXITS data provided by Shaun Johnston, 2010). To validate the new 2D model that simulated the 2D forced waves, its results are compared to the original 2D model of horizontally periodic waves in Section 4.1. After the model validation, in Section 4.2, the model of 2D forced waves is utilized to examine the evolution of internal tides on the f-plane and β-plane, based on the parameter regime from the EXperiment on Internal Tide Scattering (EXITS) observation. The simulation on the β-plane is then compared to the EXITS observation in Section 4.3. Given that the internal tides in the South China Sea primarily propagate westward along a fixed latitude, in Section 4.4, we compare the simulation on the f-plane with the observations from the P1 location. Lastly, we present the analysis of the solitary wave trains formed during the evolution of internal tides in the South China Sea in Section 4.5.

4.1 2D Horizontally periodic waves versus 2D forced waves

In this section, we show the results from the original 2D-periodic-wave model described in Section 3.1 and compare the results from the 2D-forced-wave model described in Section 3.2.

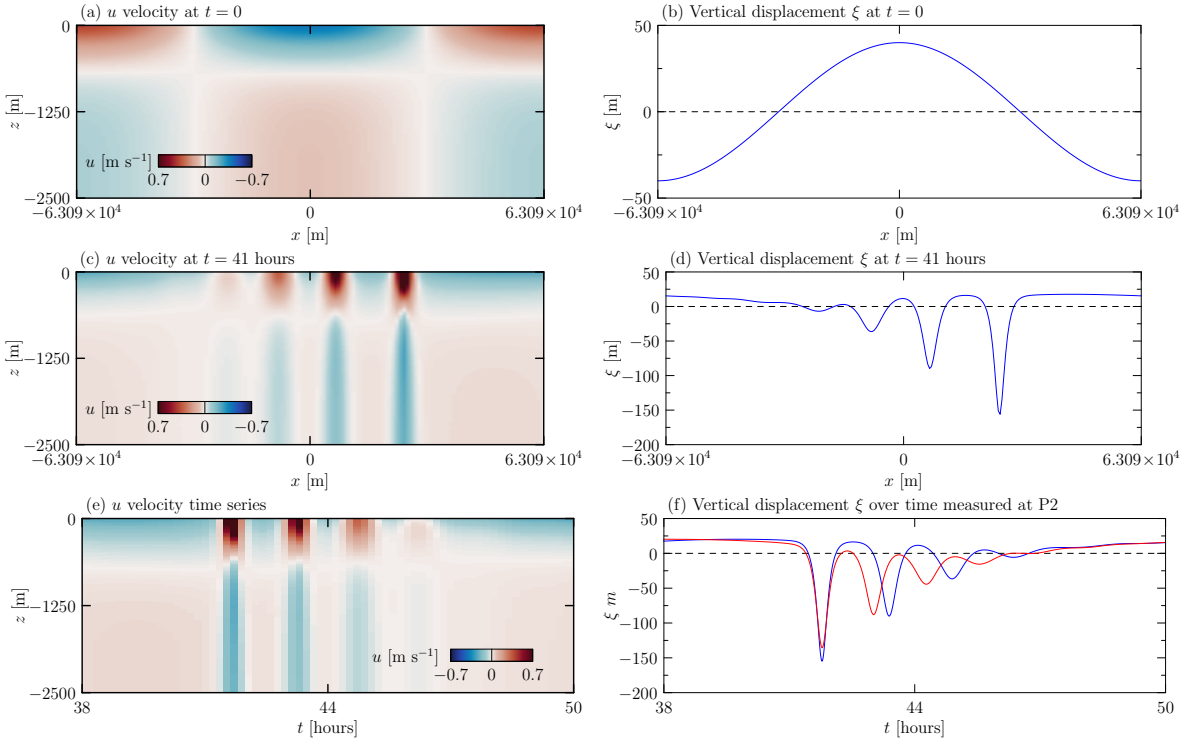

Figure 4.1: 2D horizontally periodic waves: u velocity fields and vertical displacement ξ at $z = -703$m at $t = 0$ (a & b) and $t \simeq 41$ hours (c & d), u time series at $x = 0$ (e), and vertical displacement ξ at $x = 0$ over time (f) plotted in blue, superimposed with ξ from a 2D-forced wave simulation plotted in red. The initialization or the numerical forcing used the parameter regime of the South China Sea as listed in Table 4.1 and the background stratification N^2 is given by the piecewise exponential (2.26) with the parameters listed in Table 2.2.

Parameters	Symbols	Values
Ocean depth	H	2500 m
Maximum buoyancy frequency	N_0	$N_0 = 0.0157$ s^{-1}
Initial vertical displacement amplitude	A_0	40 m
Frequency of internal tides	ω	0.000144 s^{-1}
Wavenumber of internal tides	k	0.000048 m^{-1}
Coriolis parameter	f_0	0.00005181 s^{-1}

Table 4.1: Parameter regime of the South China Sea. Here, H and N_0 were chosen from the observations (see Section 2.2.2), A_0 was estimated from the amplitude of solitary waves in the South China Sea, ω and k were the typical values for the internal tides in the South China Sea, and f_0 was calculated based on the latitude $\theta_0 \simeq 21°$.

Using the model of horizontally periodic waves described in Section 3.1, the u velocity field at $t = 0$ for one wavelength of the 2D horizontally periodic wave (see Figure 4.1(a)) was initialized using the parameter regime of the South China Sea as listed in Table 4.1. The background stratification N^2 was constructed by the piecewise exponential (2.26) with the parameters listed in Table 2.2. The corresponding vertical displacement shown in 4.1(b) is plotted at $z = -703$m which is the depth of maximum streamfunction and inflection of u. Figure 4.1 (c) and (d) show the stage at a later time, $t = 41$ hours, which is the time predicted for the waves to reach the P2 location in the South China Sea (see Figure 1.4). At this time, a solitary wave train formed, resulting from the superposition of the superharmonics.

Figure 4.1 (e) and (f) illustrate the time series of the u field and ξ over one semi-diurnal period between 38 and 50 hours after the start of the simulation. For comparison, we also performed a simulation of a forced wave with the same parameters on the f-plane, as described in Section 3.2. The forced wave is predicted to reach the P2 location after propagating for $\simeq 41$ hours, so we examine ξ of the horizontally periodic wave after this 41-hour evolution. The vertical displacement ξ of the forced wave is plotted in red in Figure 4.1(f) for comparison with the horizontally periodic case in blue. It was measured at the P2 location and at the same depth. The start of the time series of the forced waves was taken to be $t_0 = 57$ hours to account for the time over which the forcing increased to its prescribed maximum (see Section 3.2.1). Compared to the horizontally periodic waves, the forced waves exhibited an equal number of peaks and a comparable magnitude of ξ within the solitary wave train. However, the distance between the trailing downward peaks in the solitary wave train is smaller for the forced wave than for the initially-periodic wave. Overall, we find the 2D model for forced waves qualitatively and somewhat quantitatively reproduces the results obtained from the original 2D-periodic-wave model.

4.2 Effect of β-plane

As anticipated by theory, the evolution of internal tides behaves differently on the β-plane than on the f-plane. In particular, we expect solitary wave trains to develop more rapidly and to grow to larger amplitude with more waves in the wave train as the Coriolis parameter

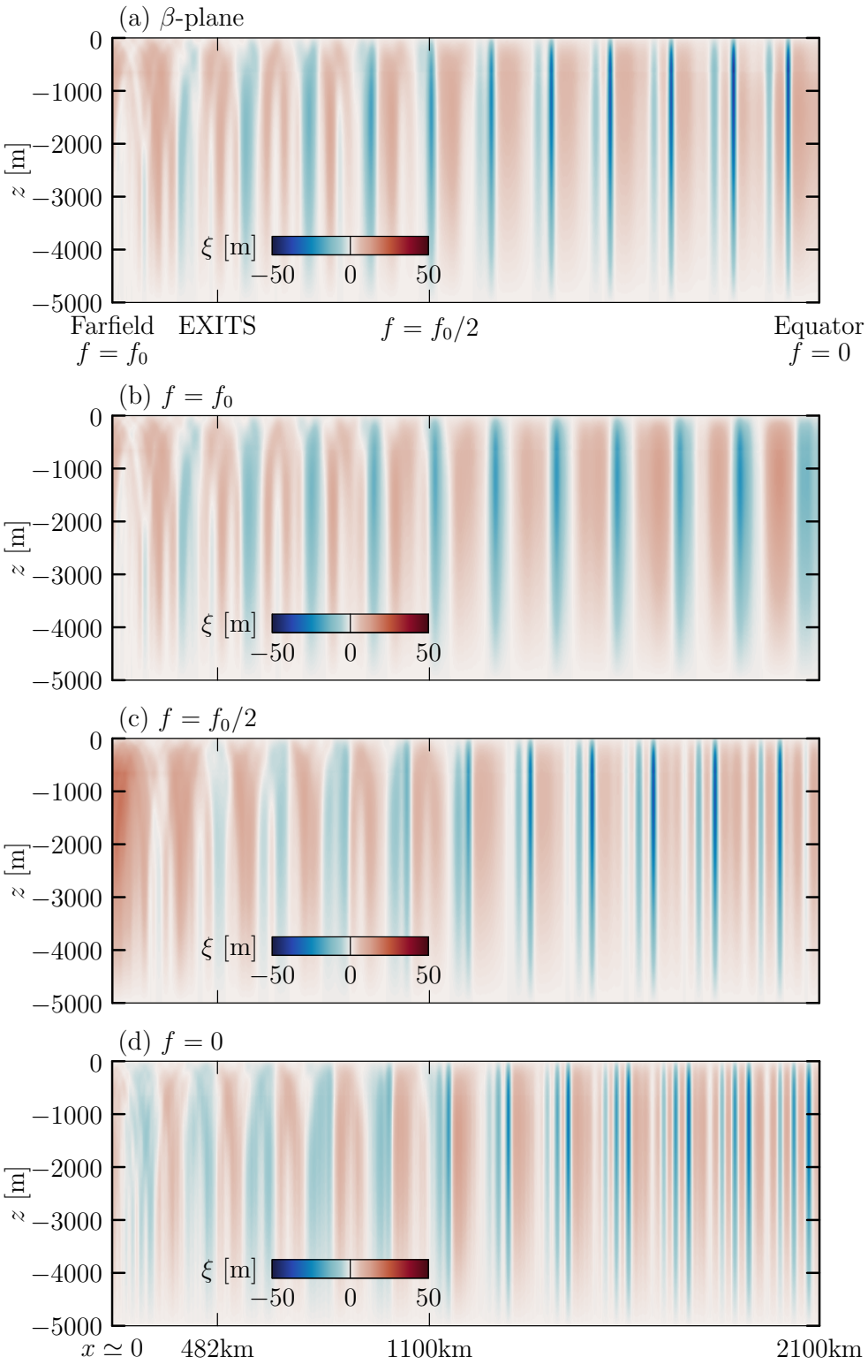

Figure 4.2: Comparison of the vertical displacement fields, ξ, of the internal tides originated from the Hawaiian Ridge evolving on the β-plane and on the f-plane with different Coriolis parameters. The constant Coriolis parameter $f_0 \simeq 4.6 \times 10^{-5}\text{s}^{-1}$ set based on the Farfield location, ocean depth $H = 5000$m, forcing amplitude $A_0 \simeq 15$m, and the background stratification was set up using the piecewise exponential (2.26) fitted to the observation dataset from EXTIS, as plotted in Figure 2.1.

f becomes smaller (Sutherland and Dhaliwal, 2022). Because this study is motivated by the observed internal tide that propagated southwest Hawaii toward the equator, we use the stratification from the EXITS observation measured about 1000km southwest Hawaii (Shaun Johnston, 2010).

The simulated vertical mode-1 internal tides originated near the Hawaiian Ridge and propagated southwest towards the equator. In the β-plane simulations, f is given by (2.17) with $f_0 \simeq 4.60 \times 10^{-5}\mathrm{s}^{-1}$ and $\beta_x \simeq 1.88 \times 10^{-11}(\mathrm{m\,s})^{-1}$. The constant Coriolis parameter, f_0, was set based on the location of the Farfield site (see Figure 1.1) where the waves were observed to propagate horizontally with a dominant vertical mode-1 structure. For the f-plane simulations, we treated f as constant and ran three cases with $f = f_0$, $f_0/2$, and 0.

Figure 4.2 compares the evolution of waves on the β-plane with different cases on the f-plane mentioned above. The results are presented by the vertical displacement fields from the simulations of the 2D-forced waves (as described in Section 3.2). Only the domain of interest is shown here. Figure 4.2(a) shows the results of the simulation on the β-plane where the Coriolis parameter decreases continuously towards the equator. Solitary waves began to show up after the waves propagated half way along the domain and formed a solitary wave train with large vertical displacements of $\simeq$ 51m near the equator. In a simulation with a relatively large constant Coriolis parameter ($f = f_0$) on the f-plane (Figure 4.2(b)), the signals of solitary waves were weak and no solitary wave train formed. If $f = f_0/2$ (Figure 4.2(c)), solitary wave trains began to form half way along the domain and peaks within the wave train grew stronger, eventually resulting a maximum vertical displacement of $\simeq$ 30m in the ocean. For $f = 0$, illustrated in Figure 4.2(d), solitary wave trains showed up quickly after the waves propagated away from the generation location and successive peaks became distinct with the vertical displacement around 30m. Though the maximum vertical displacement with $f = 0$ is similar to that with $f = f_0/2$, there are more peaks in a solitary wave train with $f = 0$ as the waves are approaching the equator, indicating more significant signals of solitary waves.

The results demonstrate that in a more realistic simulation with the β-plane employed, solitary wave trains could form as the internal tides originated from the Hawaiian Ridge approaching the equator. However, neither observations nor satellite images have seen evidence

for the internal tide transforming into solitary waves. One possible reason is that when propagating over elevated submarine topography (e.g. the Line Ridge, located closely southwest of the EXITS site), the mode-1 waves are scattered into dominant mode-2 waves which are less likely to form solitary waves, as noted in the unpublished report from EXITS by Shaun Johnston (2010).

4.3 EXITS observation versus simulation

As described in Section 1.2.2, EXITS performed ocean measurements near the Line Ridge, about 1000km southwest of Hawaii (unpublished data provided by Shaun Johnston, Scripps Institution of Oceanography). From the measured potential density field, we computed the corresponding vertical displacement of isopycnals, which are plotted in Figure 4.3(a). We chose the location at 17.61°N and 168.51°W which was located before the tides interacted with the leading flank of the Line Ridge (see Figure 1.2). The time window of the observations started at UTC 22:13, Nov 26th 2010. From this time, we traced back when the tides were generated at the Hawaiian Ridge and determined the tidal phase at that time. Predicting the M_2-generated internal tides propagated at a constant group velocity $c_g \simeq 3.1\text{ms}^{-1}$, they would arrive at the EXITS observation site after propagating for about 43 hours from the Farfield. At this time, the internal tides at the Hawaiian Ridge were generated by the spring tide, according to National Oceanic and Atmospheric Administration (NOAA). At the Farfield site, the corresponding vertical mode-1 waves during the spring tide had a half peak-to-peak vertical displacement of isopycnals $\simeq$ 25m. The numerical forcing was thus utilized to force the mode-1 waves with this amplitude at the modelled Farfield site ($x = 0$ in the domain). The simulation results measured at the location corresponding to the EXITS observation site are shown in Figure 4.3(b). The vertical displacement from the observation and simulation at the depth $z = -300$ are compared in Figure 4.3(c). The simulated internal tides formed relatively weak solitary waves with a downward vertical displacement, $|\xi_{\text{min}}|$, about 40m, as shown in the blue line in Figure 4.3(c). There was a downward peak revealed by the observation with $|\xi_{\text{min}}| \simeq 40$m at about 7.5 hours as shown in red in Figure 4.3(c), which was almost the same compared to the simulation. However, the structure of solitary waves was not clearly seen in

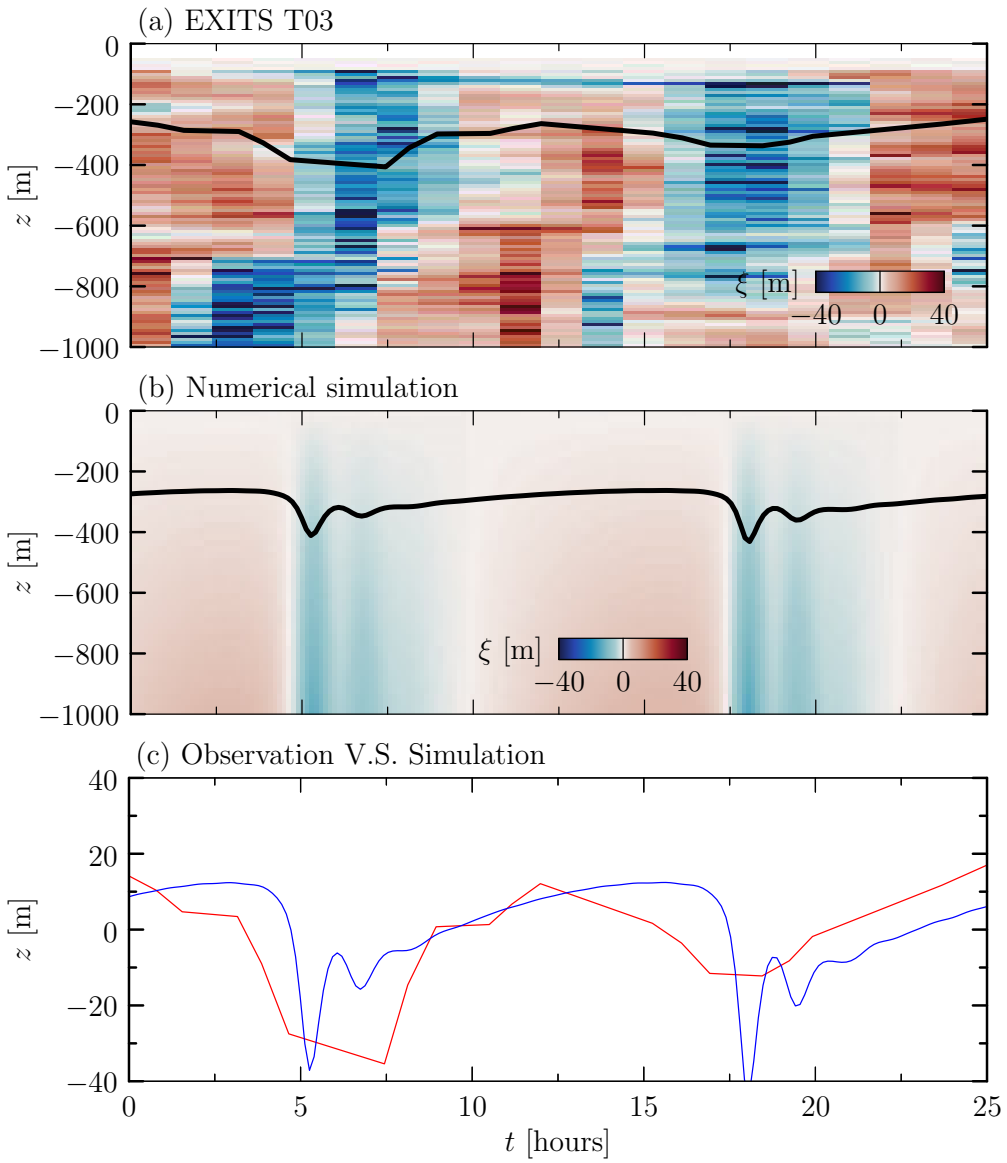

Figure 4.3: Comparison of the vertical displacement fields, ξ, from the EXITS observation and the simulations on the β-plane with the following parameters: ocean depth $H = 5000$m, forcing amplitude $A_0 \simeq 15$m, and the background stratification based on the piecewise exponential (2.26) fitted to the observation dataset from EXTIS, as plotted in Figure 2.1. The observation was performed at 17.61°N and 168.51°W starting from UTC 22:13 Nov 26th (unpublished data provided by Shaun Johnston, Scripps Institution of Oceanography). The thick black lines in (a) and (b) indicate ξ at $z = -300$m, which were compared in (c) with observation data plotted in red and simulation results plotted in blue.

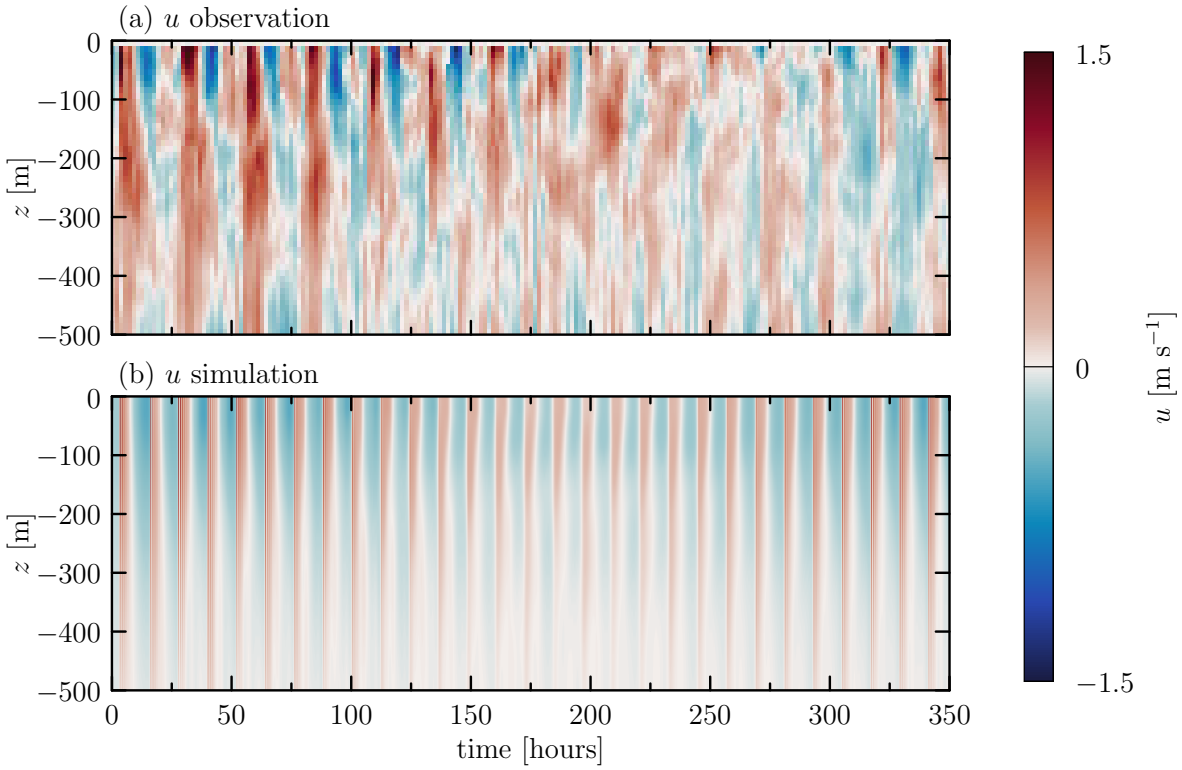

Figure 4.4: Comparison of the time series of the u velocity from the surface to $z = -500$m between the observation (a) and simulation (b). The observation was taken near the P1 location in the South China Sea at 20.71°N and 120.45°E during UTC June 14th to July 1st 2011. Simulation results are measured at the location in the model domain corresponding to the P1 location. Ocean depth in the simulation is set to $H = 3000$m according to the measured ocean depth at the P1 location. Other parameters are set based on the parameter regime of the South China Sea as listed in Table 4.1 and the background stratification N^2 is given by the piecewise exponential (2.26) with the parameters listed in Table 2.2.

the observation, with only a downward peak observed at around 7.5 hours. Among several factors, this discrepancy may be attributed to observational limitations, such as insufficient time resolution and the lateral spreading of the realistic waves that were not captured by the 2D model (though see Chapter 5).

4.4 Observation versus simulation in the South China Sea

The in-situ measurements of velocity and stratification near the P1 location in the South China Sea (see Figure 1.4) were conducted by Johnston et al. (2013). From these, we extracted the observed u velocity time series from the surface to a depth of $z = -500$m, which is plotted in Figure 4.4(a). This is compared to the simulation shown in Figure 4.4(b) from the model of the 2D-forced waves described in Section 3.2. The simulation used the ocean depth, $H = 3000$m,

according to the measured ocean depth at the P1 location. Since the internal tides in the South China Sea propagate mainly westward along a fixed latitude, the f-plane approximation was adopted here. The amplitude modulation in the numerical forcing described in Section 3.2.1 was included to simulate a more realistic internal tide between spring and neap cycles. The tidal phase in both the observations and simulations was adjusted to start at the spring tide.

With a mixed signal of semi-diurnal tide and diurnal tide, the observed waves have a smaller frequency than the simulated semi-diurnal tide. The observation still shows a strong signal of solitary waves forming, resulting in the narrow and large peaks in the u time series, particularly during the phase of largest-amplitude internal tides ($0 \lesssim t \lesssim 125$ hours). The simulation also shows a similar pattern of solitary waves with comparable magnitude. However, because the simulated waves are purely semi-diurnal, the solitary waves have narrower peaks. As the amplitude decreases and the tides enter neap phase, the signal of solitary waves diminishes in both the observation and simulation. After around 300 hours ($\simeq$ 13 days), the simulation shows a significant growing signal of solitary waves as the wave amplitude increases. However, in the observation solitary waves have only weakly redeveloped at this time, as indicated by a narrowing duration of positive u being apparent at about 325 hours. The discrepancy between simulation and observation primarily arises from the longer modulation period in the observation due to the mixed signals of semi-diurnal and diurnal tides; in the simulation the modulation period was precisely set at 14 days, and only semi-diurnal tides were simulated.

4.5 Solitary wave analysis

It is well-documented that solitary wave trains form in the South China Sea during the westward propagation of internal tides generated at the Lan Yu Ridge and Heng Chun Ridge. Consequently, this region has been extensively examined by observational oceanographers. Therefore, we chose the South China Sea as the domain for our simulations to investigate the formation of solitary wave trains. Our models require a constant ocean depth H, but H changes in reality. In the South China Sea, H decreases from 3000m at the generation site

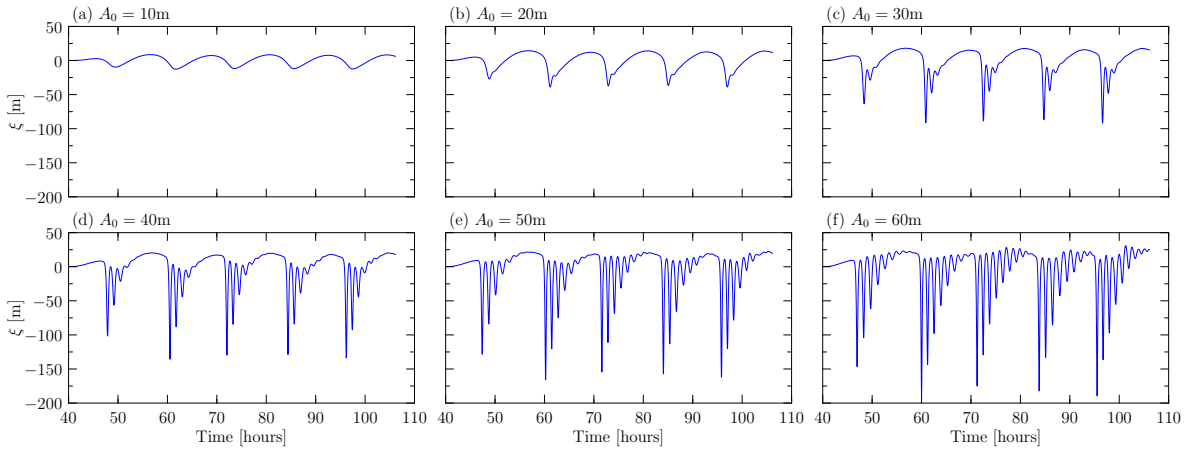

Figure 4.5: Vertical displacement ξ over time measured at the P2 location and $z = -703$m as it depends on the scaled amplitude of the numerical forcing A_0: (a) 10m, (b) 20m, (c) 30m, (d) 40m, (e) 50m, and (f) 60m. Other parameters are kept constant based on the parameter regime of the South China Sea listed in Table 4.1 and the background stratification N^2 is given by the piecewise exponential (2.26) with the parameters listed in Table 2.2. In all cases, the time series starts at 40 hours, being the time for waves to travel from the forcing location to P2.

of the internal tides to 1500m over a westward distance $\simeq$ 440km. Thus we vary H as well as forcing amplitude in different simulations to explore their influence on the excitation of solitary waves. In these experiments, we used the same background stratification N^2, given by the piecewise exponential (2.26) with the parameters listed in Table 2.2. The simulations were conducted using the 2D-forced-wave model described in Section 3.2. Waves were forced at $x = 0$, and their structure was examined at $x = 287.5$km corresponding to the observation site P2 (see Figure 1.4).

Figure 4.5 shows the vertical displacement, ξ, over time, measured at the P2 location and at depth $z = -703$m, from simulations with different amplitudes of the numerical forcing. At time $t = 0$, the forcing began to generate waves which propagated rightward in the domain reaching the P2 location after approximately 41 hours as predicted by the time to travel to P2 at the horizontal group velocity. Starting with small forcing amplitudes, solitary waves did not form in (a) and barely formed in (b) because the forcing amplitudes were so small that the nonlinear effects were very weak. In the simulation for which the forcing amplitude was increased to $A_0 = 30$m (Figure 4.5(c)), solitary wave trains began to form, having two or three peaks in a wave train, and the magnitudes of displacement for these peaks grew to over 100m. This result is comparable to the observed number of peaks in a solitary wave train and

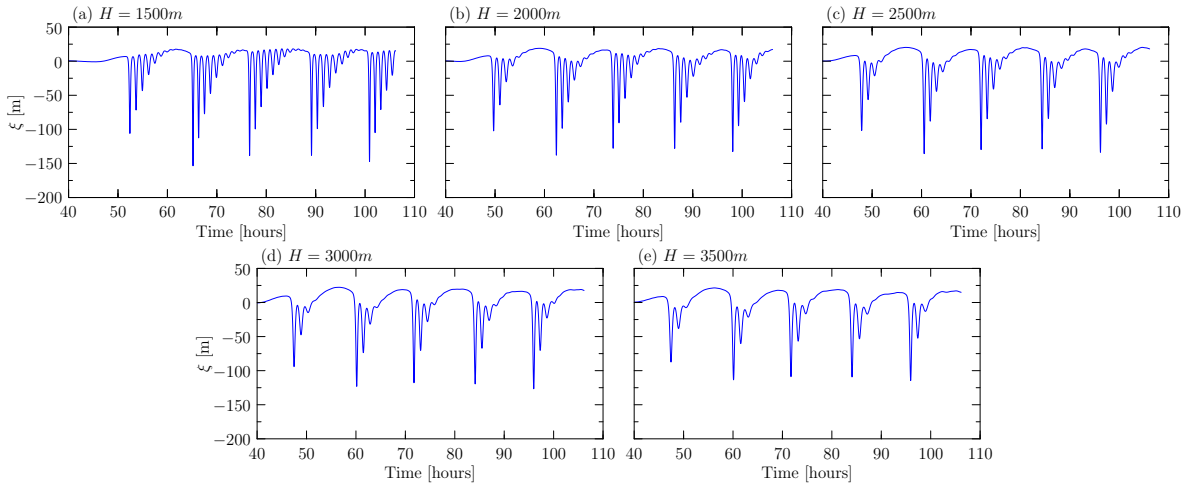

Figure 4.6: Vertical displacement ξ over time measured at the P2 location and $z = -703$m as it depends on the simulated ocean depth H: (a) $H = 1500$m and $k \simeq 5.73 \times 10^{-5}$m^{-1}, (b) $H = 2000$m and $k \simeq 5.30 \times 10^{-5}$m^{-1}, (c) $H = 2500$m and and $k \simeq 4.96 \times 10^{-5}$m^{-1}, (d) $H = 3000$m and $k \simeq 4.90 \times 10^{-5}$m^{-1}, and (e) $H = 3500$m and $k \simeq 4.86 \times 10^{-5}$m^{-1}. Other parameters are kept constant based on the parameter regime of the South China Sea listed in Table 4.1 and the background stratification N^2 is given by the piecewise exponential (2.26) with the parameters listed in Table 2.2. In all cases, the time series starts at 40 hours, being the time for waves to travel from the forcing location to P2.

the maximum wave amplitude of 155m in the South China Sea at the P2 location as shown in Figure 1.4 (Farmer et al., 2009). In simulations with larger forcing amplitude, more peaks in the solitary wave train formed and the magnitude of vertical displacement grew dramatically, as shown in (d)-(f).

Figure 4.6 shows the vertical displacement ξ at the same location from a series of simulations in which the model ocean depth H had values between 1500m and 3500m. In these simulations, the variation in depth reflects the real-world range of ocean depths in the South China Sea where H decreases from over 3000m at the internal tides' generation site to 1500m approximately 444km westward. The observation locations, P1 and P2 (see Figure 1.4), were situated in waters with depths of 3000m and 2000m, respectively. Other parameters are kept constant in these five simulations. However, the internal tide frequency, ω, given by (2.29) depended on the given wavenumber k, which is scaled by H in the model. To ensure that we always force the semi-diurnal tides at the fixed frequency, $\omega \simeq 0.000145$s^{-1}, we adjusted the wavenumber k to keep the same wave frequency in the five simulations with different values of H. Consequently, the corresponding wavelength varied from 110km to 130km in these simulations. This change in the wavelength of internal tides is reasonable as they are

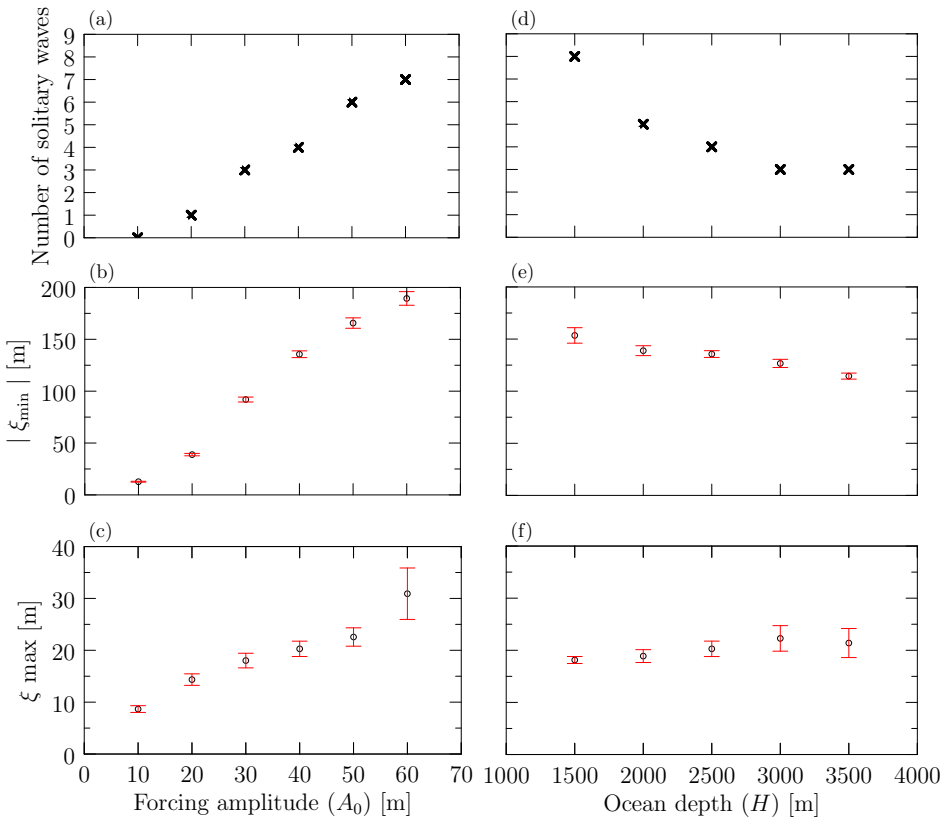

Figure 4.7: Dependence of number of waves (a, d) in a solitary wave train and the magnitude of maximum (c, f) and minimum (b, e) vertical displacement on the numerical forcing amplitude and ocean depth from 2D simulations. Ocean depth $H = 2500$m in (a), (b), and (c). Forcing amplitude $A_0 = 40$m in (d), (e), and (f). Other parameters are set constant based on the parameter regime of the South China Sea as listed in Table 4.1 and the background stratification N^2 is given by the piecewise exponential (2.26) with the parameters listed in Table 2.2. Error bars are shown in red.

observed to have a wavelength $\simeq$ 100km in the South China Sea (Farmer et al., 2009). The results are shown in Figure 4.6.

In shallower water, the signals of solitary wave trains were extremely strong, with over six peaks in a wave train and downward displacements larger than 150m, as shown in Figure 4.6(a). In the simulations with a deeper ocean, the signals of solitary wave trains became weaker, exhibiting fewer peaks in the wave train and slightly smaller downward displacement.

From the results in Figure 4.5 and 4.6, the dependence of number of waves (peaks) in a solitary wave train and the magnitude of maximum (ξ_{max}) and minimum ($|\xi_{min}|$) vertical displacement on the forcing amplitude and ocean depth is summarized in Figure 4.7. From (a) to (c), both the number of peaks in a wave train and the amplitude of the peaks, especially $|\xi_{min}|$, increase significantly with forcing amplitude, demonstrating that the strength of soli-

tary wave trains depends significantly on the forcing amplitude of the parent wave. This result is expected since a parent wave with larger amplitudes will cause stronger nonlinear effects resulting in stronger solitary waves forming during the evolution. Interestingly, (d) reveals that the number of peaks decreases nearly asymptotically to three peaks with increasing ocean depth. However, from (e) and (f), both the maximum and minimum vertical displacements appear to be relatively insensitive to the variations in ocean depth in the 2D simulations. As illustrated by the error bars in Figure 4.7 (c) and (f), the deviation of maximum vertical displacement increases with increasing A_0 and H, due to larger fluctuations of $\xi_{\max}$.

Chapter 5

3D Simulation Results

In this chapter, simulation results from the 3D model described in Section 3.4 are presented. Although the simulations were performed with nondimensional parameters based on depth scale, H, and time scale, N_0^{-1}, the results here are given in dimensional units relevant to observations in the South China Sea. To begin with, results from the 3D model are compared to those from the 2D model simulating the horizontally periodic waves described in Section 3.1. In Section 5.2, the solitary waves from the 3D simulations are analyzed and compared with those from the 2D simulations. Lastly, the characteristics of the spanwise evolution is discussed in Section 5.3.

5.1 3D versus 2D horizontally periodic waves

In this section, we compare the simulations of the horizontally periodic waves from the 2D model described in Section 3.1 and the 3D model described in Section 3.4.

The background stratification N^2 is constructed by the piecewise exponential (2.26) with the parameters listed in Table 2.2. We use the parameter regime of the South China Sea as listed in Table 4.1. The initial states of the u velocity field and vertical displacement ξ at $z = -703$m for one wavelength of the 3D horizontally periodic wave are shown in Figure 5.1 (a) and (b). The depth $z = -703$m is associated with the peak of the streamfunction and the inflection point of the u velocity. Compared to the 2D waves shown in Figure 4.1 (a) and (b), the initial vertical profile of u at $y = 0$ for the 3D wave is identical to that for the 2D waves

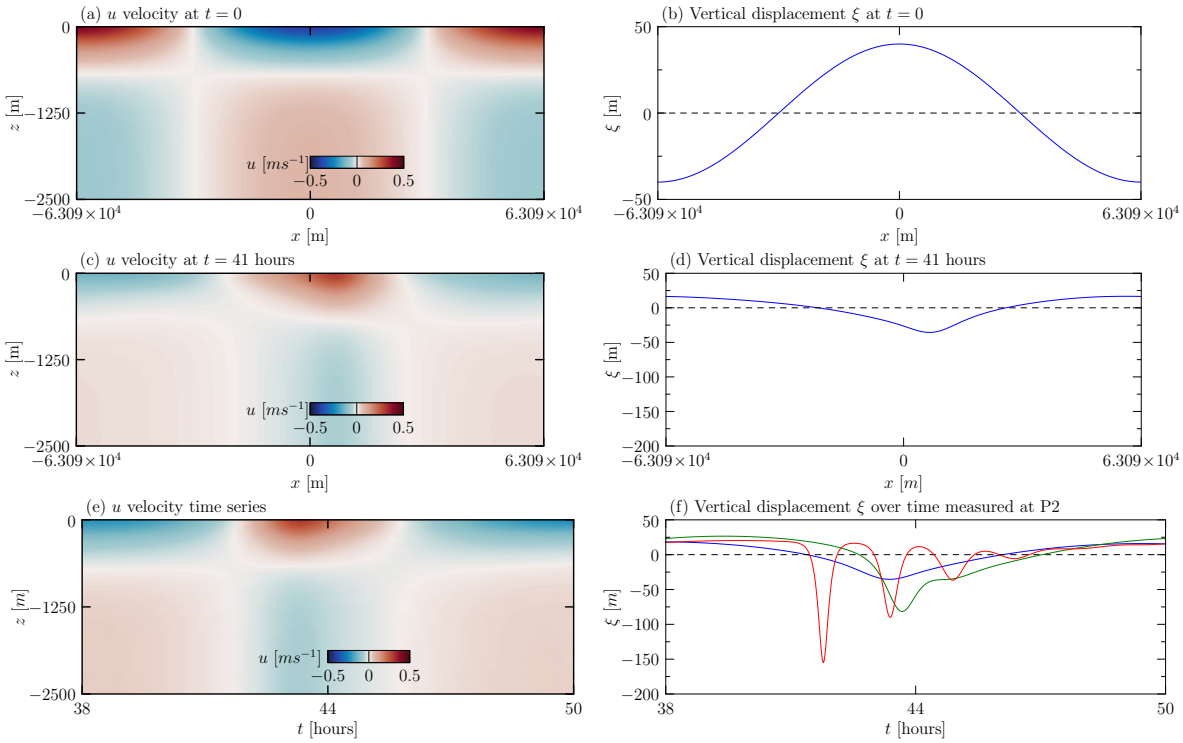

Figure 5.1: 3D horizontally periodic waves with a spanwise width of $\sigma_y = 50$km: u velocity field and vertical displacement at $t = 0$ (a & b) and $t = 41$ hours (c & d), u time series at $x = 0$ (e), and vertical displacement ξ at $x = 0$ over time (f) plotted in blue, superimposed with ξ from another 3D waves with $\sigma_y = 150$km plotted in green and a 2D horizontally periodic wave plotted in red. ξ was taken from $z = -703$m. The initialization used the parameter regime of the South China Sea as listed in Table 4.1 and the background stratification N^2 is given by the piecewise exponential (2.26) with the parameters listed in Table 2.2.

in the streamwise direction as expected. However, in the 3D simulation, the lateral width of the waves is finite with $\sigma_y = 50$km.

After evolving for 41 hours, which is the time predicted for the waves to reach the P2 location in the South China Sea (see Figure 1.4), the steepening of the wave trough associated with the initiation of solitary waves is evident by the u velocity field and vertical displacement in Figure 5.1 (c) and (d).

Figure 5.1 (e) and (f) illustrate the time series of the u field and ξ measured at the P2 location over one semi-diurnal period between 38 and 50 hours from the start of the simulation. For comparison, ξ measured at the same location and depth from another 3D wave with $\sigma_y = 150$km and a 2D wave simulated using the same parameters is plotted in green and red in Figure 5.1 (f), respectively. The comparison clearly demonstrates a much weaker signal of solitary waves in the 3D wave, due to the lateral dispersion caused by the spanwise spreading of the 3D wave. For the 3D wave with a larger spanwise width of $\sigma_y = 150$km, the dispersion by the spanwise spreading is slower, indicated by a stronger signal of solitary waves forming. The influence of lateral spreading in the spanwise direction on the formation of solitary wave trains will be examined in the next section.

5.2 Solitary wave analysis

Built on the analysis of solitary waves in the 2D simulations presented in Section 4.5, we quantitatively compare the 3D results with 2D results in terms of the solitary waves in this section. We used the same parameter regime of the South China Sea as the 2D simulations for the 3D ones presented in this section. Also, the background stratification N^2 in the 3D simulations was identical to that used in the 2D simulations, described by the piecewise exponential (2.26) with the parameters in the South China Sea listed in Table 2.2.

To investigate the dependence of solitary waves on the amplitude of the parent wave, we varied the initial vertical displacement amplitude, A_0, in the 3D model for a series of simulations. Again, we measured the vertical displacement, ξ, at $z = -703$m and the P2 location in the South China Sea (see Figure 1.4). The P2 location was estimated based on the travel time of the waves (see Section 3.4.5). The spanwise width of the waves was fixed at

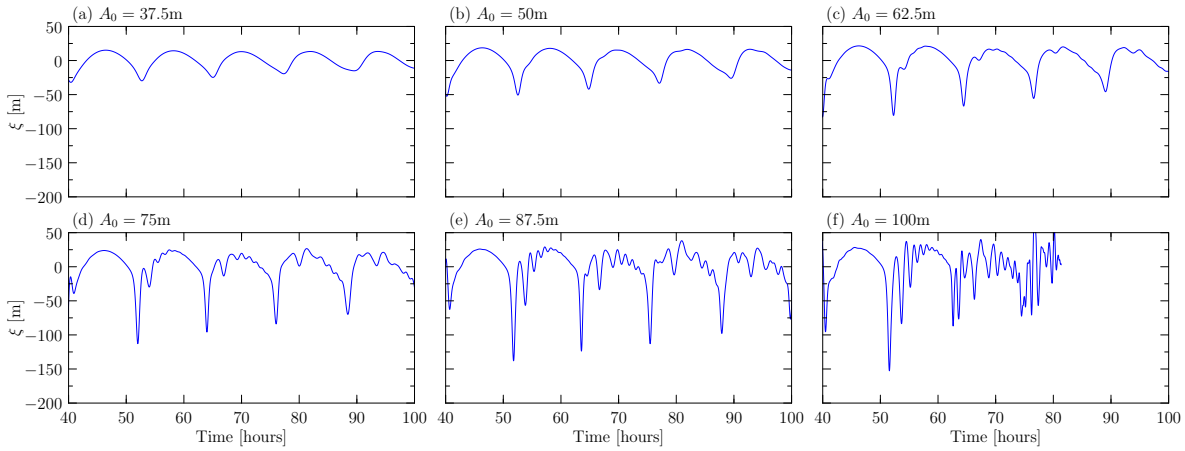

Figure 5.2: Vertical displacement ξ over time measured at the estimated P2 location as it depends on the initial maximum vertical displacement A_0: (a) 37.5m, (b) 50m, (c) 62.5m, (d) 75m, (e) 87.5m, and (f) 100m. Other parameters are kept constant based on the parameter regime of the South China Sea listed in Table 4.1 and the background stratification N^2 is given by the piecewise exponential (2.26) with the parameters listed in Table 2.2. In all cases, the time series starts at 40 hours, being the time for waves to travel from the forcing location to the estimated P2 location for the 3D horizontally periodic waves.

$\sigma_y = 50$km and the ocean depth was $H = 2500$m. Other parameters were held constant and identical to those for the 2D-wave simulations shown in Figure 4.5. The simulation results are shown in Figure 5.2.

Due to lateral dispersion, as the waves propagate their centreline amplitude at $y = 0$ decays. This explains why the solitary waves are not so pronounced in the simulations of the relatively small-amplitude waves, as shown in Figure 5.2 (a) and (b). A strong signal of localized and deep solitary waves is evident when the initial vertical displacement amplitude, A_0, is 62.5m, as shown in Figure 5.2(c). The amplitude of these solitary waves is comparable to the 2D results in Figure 4.5 (c) in which A_0 is only 30m. As we further increase the initial amplitude, the vertical displacement of the solitary waves, especially the maximum downward displacement, $|\xi_{\min}|$, grows significantly. This trend is expected and similar to the 2D results. If A_0 is 100m (Figure 5.2 (f)), nonlinear effects become so significant that the displacement becomes incoherent after 80 hours, with the code becoming numerically unstable to small-scale disturbances shortly thereafter.

To investigate the dependence of solitary waves on the ocean depth, we varied H from 2000m to 3500m in the 3D model keeping $A_0 = 75$m and $\sigma_y = 50$km fixed. The simulation with $H = 1500$m is not included here because the waves broke immediately when we began the

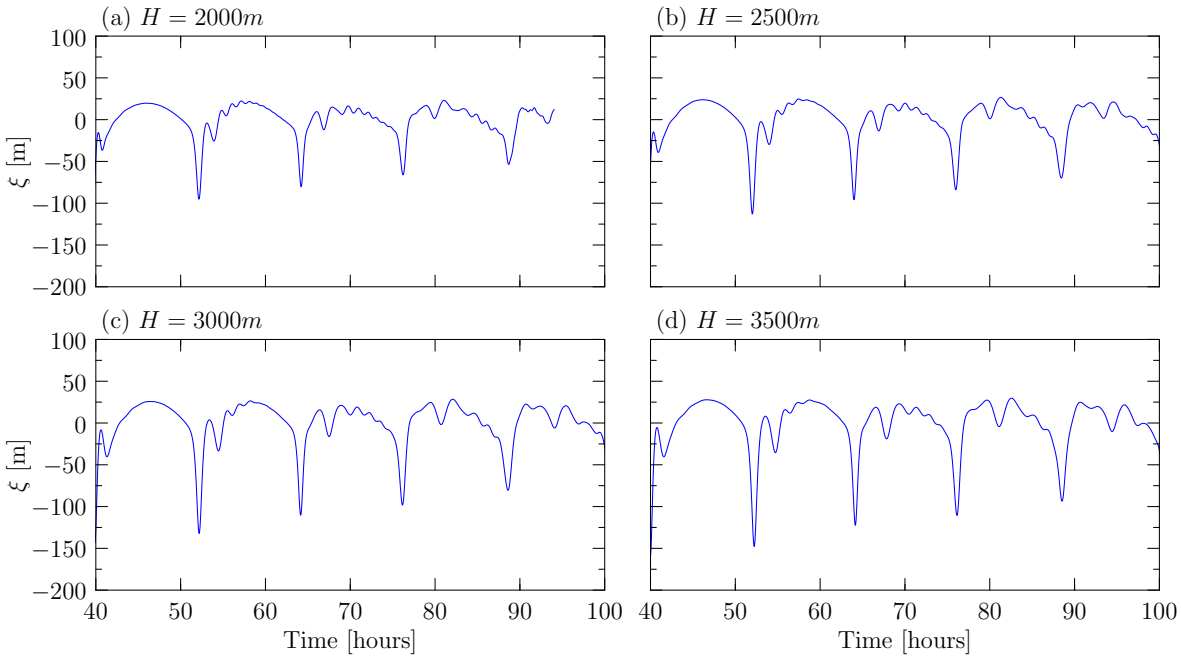

Figure 5.3: Vertical displacement ξ over time measured at the P2 location as it depends on the simulated ocean depth H: (a) $H = 2000$m and $k \simeq 5.30 \times 10^{-5}\text{m}^{-1}$, (b) $H = 2500$m and and $k \simeq 4.96 \times 10^{-5}\text{m}^{-1}$, (c) $H = 3000$m and $k \simeq 4.90 \times 10^{-5}\text{m}^{-1}$, and (d) $H = 3500$m and $k \simeq 4.86 \times 10^{-5}\text{m}^{-1}$. Other parameters are kept constant based on the parameter regime of the South China Sea listed in Table 4.1 and the background stratification N^2 is given by the piecewise exponential (2.26) with the parameters listed in Table 2.2. In all cases, the time series starts at 40 hours, being the time for waves to travel from the forcing location to the estimated P2 location for the 3D horizontally periodic waves.

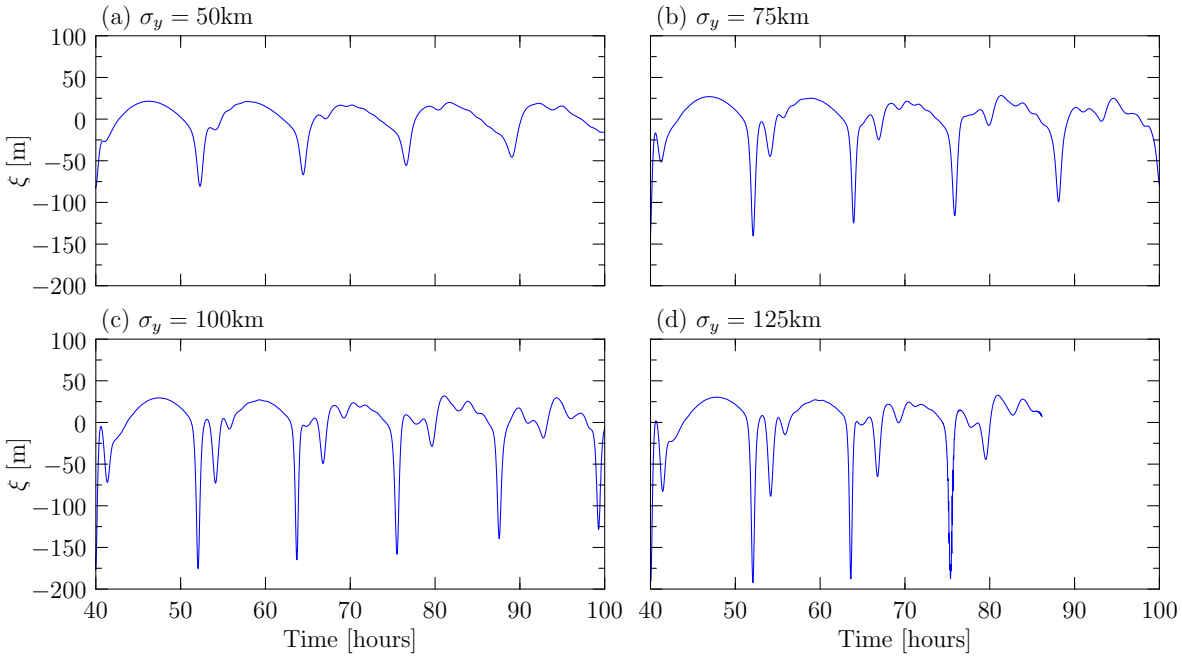

Figure 5.4: Vertical displacement ξ over time measured at the estimated P2 location as it depends on the initial spanwise width σ_y: (a) 50km, (b) 75km, (c) 100km, and (d) 125km. Other parameters are kept constant based on the parameter regime of the South China Sea listed in Table 4.1 and the background stratification N^2 is given by the piecewise exponential (2.26) with the parameters listed in Table 2.2. In all cases, the time series starts at 40 hours, being the time for waves to travel from the forcing location to the estimated P2 location for the 3D horizontally periodic waves.

measurements, due to a large relative initial amplitude $A_0/H = 0.050$ which intensified the nonlinear effects. As in the 2D models, the frequency of the waves, ω, depends on the given wavenumber k according to the eigenvalue problem in (2.29), with k scaled by H. Thus, we adjusted k in these simulations to make ω constant corresponding to the frequency of the semi-diurnal tide (see Section 4.5). Other parameters were kept constant. The vertical displacement at the depth $z = -703$m and for time after 40 hours are shown in Figure 5.3. Qualitatively, the crests of the solitary wave trains corresponding to $\xi_{\max}$ do not significantly alter with variations in ocean depth, while the maximum downward displacement $|\xi_{\min}|$ increases with increasing ocean depth. Additionally, as H increases, the crest of the solitary wave trains exhibits less small-scale oscillations, for example, at the time $t = 70 \pm 3$ hours.

To investigate the dependence of solitary waves on the initial spanwise width, we varied σ_y in the 3D model, keeping $A_0 = 62.5$m and $H = 2500$m fixed. The results for $\sigma_y = 125$km (Figure 5.4 (d)) are only shown from $t = 40$–86 hours because the waves broke hereafter. As demonstrated in Figure 5.4, when increasing σ_y, we can see larger magnitude of vertical

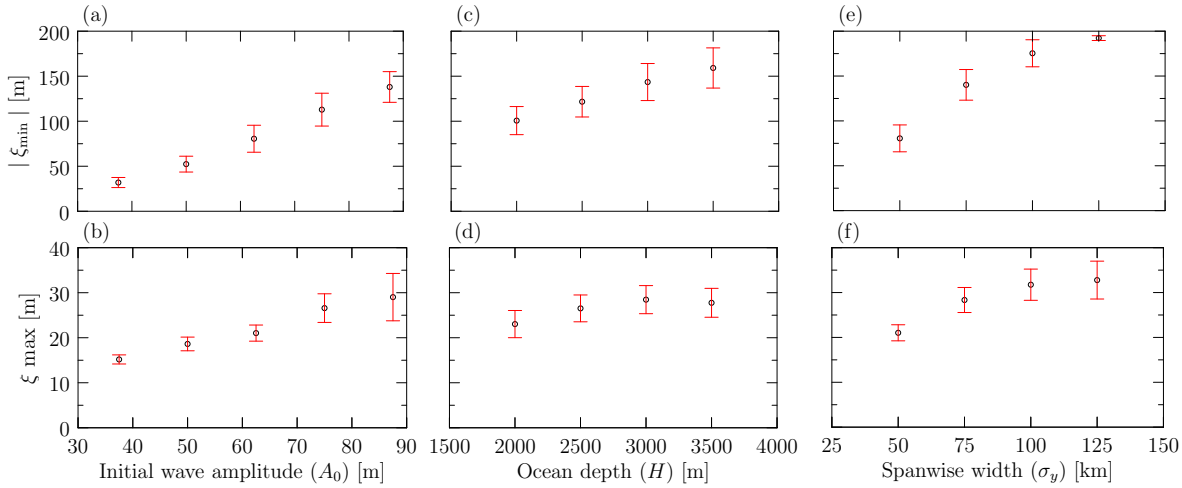

Figure 5.5: Dependence of the magnitude of maximum and minimum vertical displacement on the initial wave amplitude (a & b), ocean depth (c & d), and spanwise width (e & f) from 3D simulations. Initial wave amplitude $A_0 = 75$m in (c), (d), (e), and (f). Ocean depth $H = 2500$m in (a), (b), (e), and (f). Spanwise width $\sigma_y = 50$km in (a), (b), (c), and (d). Other parameters are set constant based on the parameter regime of the South China Sea as listed in Table 4.1 and the background stratification N^2 is given by the piecewise exponential (2.26) with the parameters listed in Table 2.2. Error bars are shown in red.

displacement from the downward peaks and more small-scale oscillations (e.g. see $t = 70 \pm 3$ hours) along the wave crest. If $\sigma_y = 125$km, the downward peaks have a vertical displacement $\simeq -200$m which is comparable to the 2D simulation with similar initial wave amplitude (see Figure 5.2 (f)). Also, during the early stages of the simulations ($t = 50$–60 hours), there are multiple distinct downward peaks without small-scale oscillations in a solitary wave train. This is similar to the structure of the 2D solitary waves except having fewer peaks. These simulations indicate more substantial amplification of solitary waves for the internal tides with larger spanwise extent, which is due to less dispersion by the spreading in the spanwise direction (to be discussed in Section 5.3).

Summarized from the results shown in Figure 5.2 and 5.3, the dependence of the minimum and maximum vertical displacement on the initial wave amplitude A_0, ocean depth H, and initial spanwise width σ_y is illustrated in Figure 5.5. This shows a similar dependence of the vertical displacement on A_0 and H to the 2D simulations. The magnitude of the minimum, $|\xi_{\min}|$, and maximum, $\xi_{\max}$, vertical displacement has a near-linear growing trend with the increasing A_0 in both the 2D and 3D simulations (Figure 5.5 (a) and (b) V.S. Figure 4.7 (b) and (c)). However, the growing trend is weaker in the 3D simulations due to the dispersion caused by the lateral spreading. In the simulations with increasing H, $|\xi_{\min}|$ moderately

increases in the 3D simulations (see Figure 5.5 (c)). This is different from the 2D simulations where $|\xi_{\min}|$ slightly decreases with increasing H. $\xi_{\max}$ varies little with increasing H in the 3D simulations (see Figure 5.5 (d)), which is consistent with the 2D simulations. In the simulations with increasing σ_y, as shown in Figure 5.5 (e) and (f), both $|\xi_{\min}|$ and $\xi_{\max}$ increase substantially. Interestingly, indicated by the error bars, the general fluctuations decrease in $|\xi_{\min}|$ but increase in $\xi_{\max}$ as we increase σ_y.

The most noticeable difference between the 2D and 3D simulations in terms of the solitary wave trains is their structure. Compared to the 2D simulations, there are fewer peaks with less dramatic downward displacement in a solitary wave train in the 3D simulations. From the simulations shown in Figure 5.2(d)–(f) and Figure 5.3(a)–(d), a crest of a solitary wave train is typically followed by only two peaks. The first peak is weak, and the second one is very strong which always exhibits the greatest $|\xi_{\min}|$ among other oscillations in a solitary wave train. As for the crests, they display more small-scale fluctuations compared to the 2D simulations, and the fluctuations are stronger if the initial wave amplitude is larger or the ocean is shallower, as evidenced by more ripples appearing along the crests in the wave trains (e.g. see the wave crests at around $t = 70$ hours in Figure 5.2 and Figure 5.3). This is due to more significant nonlinear effects during the evolution of the waves with a larger relative wave amplitude A_0/H. The 2D solitary waves behave differently with this nonlinear effect by forming more distinct and dramatic downward peaks within a solitary wave train. Although the amplitude of the waves decays during their propagation in the 3D simulations due to the dispersion caused by lateral spreading, the amplitude of the crests remain unaffected, exhibiting a nearly constant upward vertical displacement in the solitary wave trains. However, the downward displacement exhibits the most decay. Another major difference from the 2D results is that solitary wave trains from the 3D model are more sensitive to the ocean depth in terms of $|\xi_{\min}|$ which increases with larger H in the 3D results (see Figure 5.5 (c)). This is opposite to the 2D solitary wave trains for which $|\xi_{\min}|$ decreases only slightly with increasing ocean depth H, exhibiting a weak sensitivity to the ocean depth (see Figure 4.7 (e)).

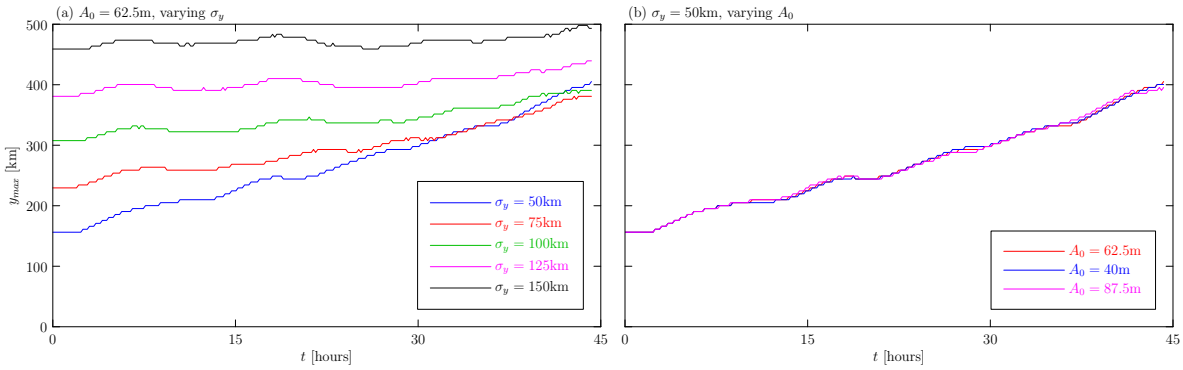

Figure 5.6: Edge of the waves, y_{max}, over time: (a) varying the initial spanwise width σ_y with the initial vertical displacement A_0 fixed and (b) varying A_0 with σ_y fixed. y_{max} is defined as where the peak surface u velocity at y is 1%. Other parameters are kept constant based on the parameter regime of the South China Sea listed in Table 4.1 and the background stratification N^2 is given by the piecewise exponential (2.26) with the parameters listed in Table 2.2.

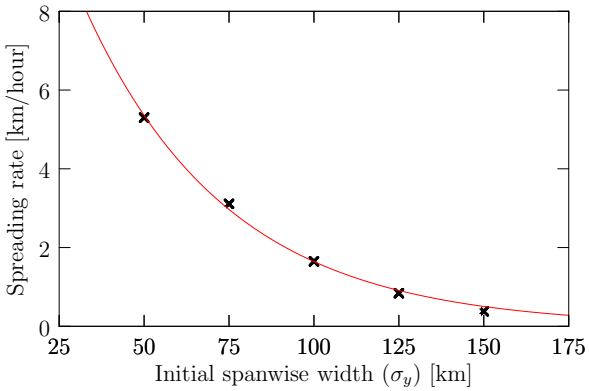

Figure 5.7: Dependence of the spreading rate, calculated by linear fitting y_{max} over time from the five simulations shown in Figure 5.6(a), superimposed with the best-fit exponential function in red.

5.3 Spanwise evolution

In this section, we focus on the spanwise evolution of waves characterized by their lateral spreading (Section 5.3.1), radius of curvature (Section 5.3.2), and the width of surface signature (Section 5.3.3). If not specified, the parameters used in the 3D simulations are based on the parameter regime of the South China Sea listed in Table 4.1. The background stratification N^2 is set by the piecewise exponential (2.26) with the parameters listed in Table 2.2.

5.3.1 Lateral spreading

Figure 5.6 demonstrates the lateral spreading over time depending on the initial vertical displacement A_0 and the spanwise width σ_y by measuring the wave edge $y_{\max}$ which is defined as where the peak surface u velocity at y is 1%. As illustrated in Figure 5.6 (a), the waves with a smaller spanwise width σ_y disperse more rapidly in the spanwise direction than those with a larger σ_y. On the other hand, with σ_y kept constant, the spreading rate does not vary with different initial wave amplitude A_0, as shown in Figure 5.6 (b). In all cases, $y_{\max}$ is able to grow to over 350km after evolving for 45 hours in an idealized ocean. Comparing this to the streamwise propagation, these internal tides with the predicted group velocity, $c_g \simeq 2.55\text{m s}^{-1}$, can propagate about 410km in the streamwise direction over 45 hours. This suggests that the range of the lateral dispersion of the internal tides is comparable with their streamwise propagation.

The increasing trend of $y_{\max}$ over time is approximately linear, allowing the calculation of the lateral spreading rate. By linear fitting $y_{\max}$ over time from the five simulations with different initial spanwise width in Figure 5.6 (a), we determine the lateral spreading rate from the slopes of these lines. These are plotted in Figure 5.7. The spreading rate shows an exponential decay with increasing initial spanwise width.

5.3.2 Radius of curvature

The radius of curvature, R_c, is a spanwise characteristic of the internal tides, resulting from the lateral bending of the surface u velocity to form an arc shape as seen from the top view on the xy-plane at the $z = 0$ (see Figure 3.6b and Section 3.4.5). From two series of simulations, we examined the dependence of R_c on the initial vertical displacement amplitude, A_0, and the spanwise width, σ_y. The results are shown in Figure 5.8, illustrating the change in R_c over time by varying one parameter while keeping the other one fixed. Other parameters were held constant. In Figure 5.8 (a), R_c starts at infinity and gradually decreases as the arc shape forms. However, after around 12 hours (one semi-diurnal period), R_c begins to increase due to the lateral spreading becoming more significant than the effect of bending. In Figure 5.8 (b), the waves with larger σ_y tend to bend (so that their R_c decreases) and take the spreading

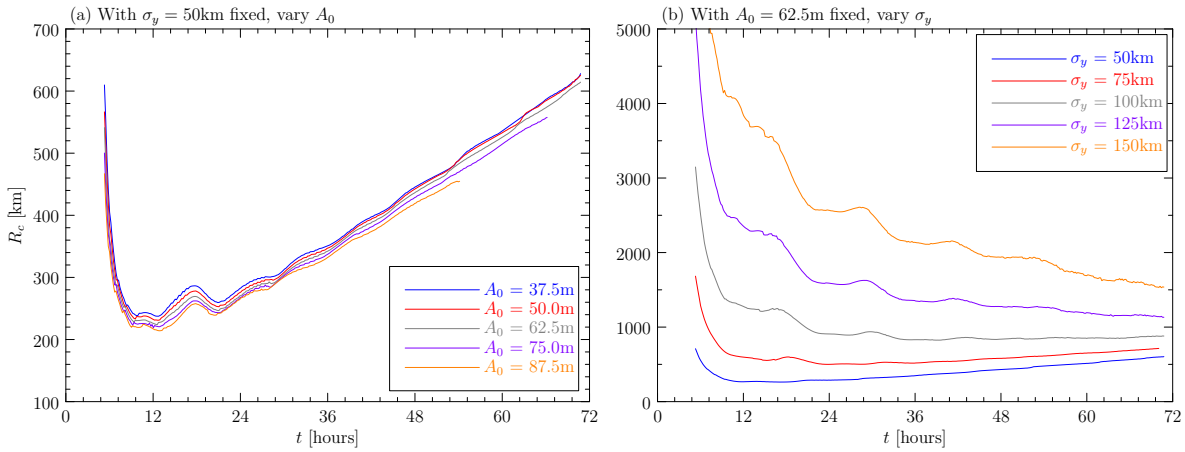

Figure 5.8: Radius of curvature, R_c, over time: (a) varying the initial vertical displacement A_0 with the spanwise width $\sigma_y = 50$km fixed and (b) varying σ_y with $A_0 = 62.5$m fixed. Other parameters are kept constant based on the parameter regime of the South China Sea listed in Table 4.1 and the background stratification N^2 is given by the piecewise exponential (2.26) with the parameters listed in Table 2.2.

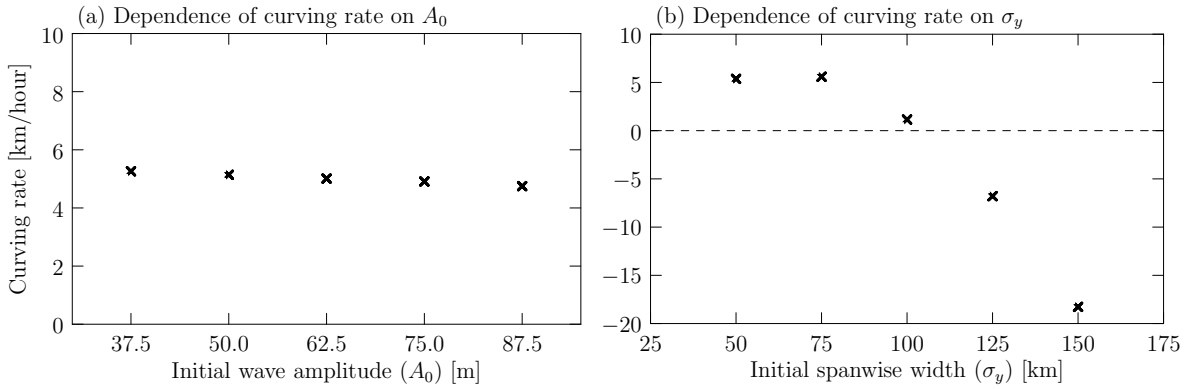

Figure 5.9: Dependence of the curving rate, calculated by linear fitting R_c over time from the two series of simulations shown in Figure 5.8

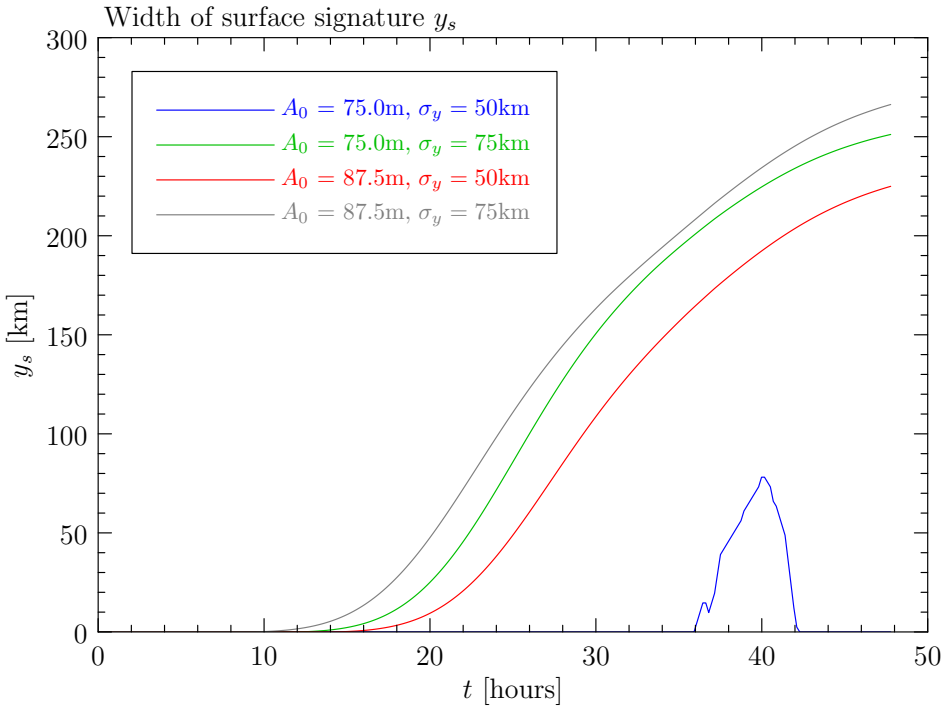

Figure 5.10: Width of surface signature, y_s, over time with the initial vertical displacement A_0 and the spanwise width σ_y in different cases. The threshold for y_s is set as $\partial u/\partial x > 2.4 \times 10^{-4}\text{s}^{-1}$. Other parameters are kept constant based on the parameter regime of the South China Sea listed in Table 4.1 and the background stratification N^2 is given by the piecewise exponential (2.26) with the parameters listed in Table 2.2.

speed longer to overtake.

We computed the slope of the nearly linear trend of R_c over time after 12 hours, which is defined as the curving rate. The results are plotted in Figure 5.9. Figure 5.9 (a) confirms that R_c does not depend on A_0. Figure 5.9 (b) shows that the curving rate does not vary much for $\sigma_y < 100$km cases. When $\sigma_y = 100$km, the curving rate $\simeq 0$ means that the effects of lateral spreading and curving are in balance after 12 hours, resulting in a steady arc shape on the xy-plane.

5.3.3 Surface signature

The evolution of the width, y_s, of the sea surface signature of internal solitary waves is determined by the surface current gradient, $\partial u/\partial x$, being larger than a threshold value ($2.4 \times 10^{-4}\text{s}^{-1}$), as described in Section 3.4.5. The results are plotted in Figure 5.10, from four simulations with different initial vertical displacement amplitude, A_0, and spanwise width,

σ_y. Although the time resolution for the computation in the simulations was set sufficiently high, the output data was saved not frequently enough from the simulations for post processing in this case. So, we smoothed the data to remove the discrete jumps in y_s.

As illustrated by Figure 5.10, the surface signature shows up after the waves have evolved for a certain time, caused by the steepening of the waves and the formation of solitary waves which intensify the surface current gradient. Apart from the results plotted here, we also examined the surface signature of the waves with the initial vertical displacement $A_0 = 87.5$m and the initial spanwise width $\sigma_y = 25$km where no surface signature was indicated by the surface current gradient. This implies that internal tides with a smaller spanwise width spread so fast that they cannot generate sufficiently large surface current convergence resulting in a visible surface signature. The waves with $A_0 = 75$m and $\sigma_y = 50$km (plotted in blue in Figure 5.10) exhibit a decay for y_s starting at $t = 40$ hours due to the lateral spreading reducing the surface current convergence. This growth and decay of the surface signature is realistic for the ocean because y_s from this simulation is close to the observed surface signature in the South China Sea. Its half-width is observed to be about 50km (see the satellite image in Figure 1.4).

The y_s values in the other three cases with large A_0 or σ_y, shown in Figure 5.10, do not decay within 50 hours as the waves maintain a sufficiently large wave amplitude that their surface current convergence remains above the threshold. However, their surface signature would decay if the simulation was run for sufficiently long time.

Chapter 6

Discussion and Conclusions

This study performed fully nonlinear simulations to examine the evolution of the low-mode internal tide as it depends on wave amplitude, ocean depth, Coriolis forces, and the spanwise extent of the waves. We began with constructing analytic non-uniform stratification profiles for use in numerical simulations by fitting a piecewise exponential function to the observed profiles near Hawaii and in the South China Sea. We then extended the 2D model of horizontally periodic waves by adding spatially localized numerical forcing of waves with amplitude modulation and rotation on the β-plane. In the simulations on the f-plane, this new 2D model of forced waves qualitatively and somewhat quantitatively agreed with the original 2D model of initially-periodic waves. Since the theory predicts that solitary waves develop more rapidly and grow to larger amplitude with a smaller Coriolis parameter, this new 2D-forced model with the β-plane configuration was useful to simulate the internal tides whose evolution extends widely from a fixed latitude. In particular, it was used to simulate internal tides which originated at the Hawaiian Ridge and propagated southwest of Hawaii towards the equator over which the Coriolis parameter decreased to zero. Using a 3D model of spanwise-localized horizontally-periodic waves, we characterized their evolution accounting for lateral spreading.

The comparison between the 2D simulation of forced waves and the EXITS observation, located about 1000km southwest of Hawaii, illustrated a fair agreement between them in terms of the vertical displacement of the isopycnals. The simulation results showed that solitary waves were able to form after travelling approximately around half the way towards the

equator. However, such formation has not been observed in situ or by satellites so far. One possible reason is that when propagating over elevated submarine topography (e.g. the Line Ridge, located closely southwest of the EXITS site), the mode-1 waves were scattered into dominant mode-2 waves which were less likely to form solitary waves, as noted in the unpublished report from EXITS by Shaun Johnston (2010). However, it could be that the waves had insufficiently small amplitude to create an observable sea-surface signature in satellite images, and the EXITS in-situ observations were too close to Hawaii for solitary waves to form.

For the South China Sea, the in-situ observation data only aligned qualitatively with the 2D simulation results. The patterns and magnitudes of the solitary waves in the observation were similar to those in the simulation. The discrepancy between them was primarily caused by different frequencies of the internal tides, and could also be due to the lateral spreading of the realistic waves that are not included in the 2D model. Nonetheless, these comparisons revealed the limitations of in-situ ocean measurements such as insufficient time resolution to capture the rapid signal of solitary waves and the potential interference from irrelevant signals.

The analysis of the solitary waves in the simulations concluded that larger amplitude internal tides result in stronger solitary waves. This was demonstrated by the increased maximum upward, $\xi_{\max}$, and particularly downward, $|\xi_{\min}|$, vertical displacements in both the 2D and 3D models. For a typical wave amplitude of 60m in the South China Sea, $|\xi_{\min}|$ was able to grow to $\simeq$ 180m in the 2D model and $\simeq$ 100m in the 3D model. These strong solitary waves were also manifest by their structure, albeit differently in the 2D and 3D models. With larger wave amplitude, the 2D model exhibited more downward peaks in the vertical displacement within a solitary wave train while the 3D model displayed more small-scale oscillations along the wave crest. For the dependence on the total depth of the ocean, H, the number of downward peaks formed by the 2D waves decreased nearly asymptotically with increasing H, while the 3D waves exhibited less small-scale oscillations. The dependence of $|\xi_{\min}|$ on H was different between the 2D and 3D waves. The solitary waves in the 2D model were not sensitive to H: $|\xi_{\min}|$ decreased only slightly with increasing H. On the contrary, in the 3D model, $|\xi_{\min}|$ was more sensitive to H, increasing with larger H. Nevertheless, the

maximum vertical displacement, $\xi_{\max}$, given by the crests of solitary waves remained almost constant in both 2D and 3D simulations. Additionally, the 3D waves demonstrated more significant growth of solitary waves for larger initial spanwise width due to reduced dispersion from the lateral spreading.

For the spanwise evolution characterized by the 3D model, we showed that the lateral spreading has a linear correlation with time. The spreading of the 3D waves was faster with smaller initial spanwise width, σ_y, while it remained the same for different values of initial wave amplitudes, A_0. The spreading rate (km per hour) decreased exponentially with increasing σ_y. A similar pattern was found in the radius of curvature, R_c, which characterized the lateral bending of internal tides from the top view. The lateral bending depends on σ_y and the waves with larger σ_y tend to keep bending for a longer time. To conclude, the spanwise evolution was mainly determined by the initial spanwise width (σ_y) rather than the initial wave amplitude (A_0).

Internal solitary waves can be visible in a satellite image by their signature of roughness on the sea surface. Our simulations from the 3D model showed a realistic evolution of this surface signature. The simulation with the initial conditions of $A_0 = 75$m and $\sigma_y = 50$km reproduces the westward propagating internal tides in the South China Sea with the good agreement with the satellite image. The initial conditions of these internal tides are barely known due to the challenging operating conditions in the Luzon Strait (Alford et al., 2015). Our 3D model allows us to estimate their initial conditions.

This study has provided approaches to more realistically simulate the evolution of internal tides by extending the 2D model to have forced waves and β-plane effect. However, our 3D model still works with the horizontally periodic waves on the f-plane. Moving forward, the numerical forcing and the β-plane can be added to the 3D model, which will increase the model's accuracy and comprehensiveness. To add the numerical forcing, one should first have two sponge layers at both ends on the xz-plane of the domain. The forcing can then be put on a slice of the yz-plane. Finally, the β-plane can be added in the x-direction.

Bibliography

Alford, M. H., J. A. MacKinnon, Z. Zhao, R. Pinkel, J. Klymak, and T. Peacock, 2007: Internal waves across the Pacific. *Geophysical Research Letters*, **34 (24)**, doi:10.1029/2007GL031566.

Alford, M. H., and Coauthors, 2015: The formation and fate of internal waves in the South China Sea. *Nature*, **521 (7550)**, 65–69, doi:10.1038/nature14399.

Alpers, W., 1985: Theory of radar imaging of internal waves. *Nature*, **314 (6008)**, 245–247, doi:10.1038/314245a0.

Baker, L. E., and B. R. Sutherland, 2020: The evolution of superharmonics excited by internal tides in non-uniform stratification. *Journal of Fluid Mechanics*, **891**, R1, doi:10.1017/jfm.2020.188.

Buijsman, M., J. McWilliams, and C. Jackson, 2010: East-west asymmetry in nonlinear internal waves from Luzon Strait. *Journal of Geophysical Research (Oceans)*, **115**, doi:10.1029/2009JC006004.

Carter, G. S., and Coauthors, 2008: Energetics of M2 barotropic-to-baroclinic tidal conversion at the Hawaiian islands. *Journal of Physical Oceanography*, **38 (10)**, 2205 – 2223, doi:10.1175/2008JPO3860.1.

Dauxois, T., S. Joubaud, P. Odier, and A. Venaille, 2018: Instabilities of internal gravity wave beams. *Annual Review of Fluid Mechanics*, **50 (1)**, 131–156, doi:10.1146/annurev-fluid-122316-044539.

Echeverri, P., M. R. Flynn, K. B. Winters, and T. Peacock, 2009: Low-mode internal tide generation by topography: an experimental and numerical investigation. *Journal of Fluid Mechanics*, **636**, 91–108, doi:DOI:10.1017/S0022112009007654.

Farmer, D., Q. Li, and J. Park, 2009: Internal wave observations in the South China Sea: The role of rotation and non-linearity. *Atmosphere-Ocean*, **47 (4)**, 267–280, doi:10.3137/OC313.2009.

Garrett, C., and E. Kunze, 2007: Internal tide generation in the deep ocean. *Annual Review of Fluid Mechanics*, **39 (1)**, 57–87, doi:10.1146/annurev.fluid.39.050905.110227.

Guo, C., and X. Chen, 2014: A review of internal solitary wave dynamics in the northern South China Sea. *Progress in Oceanography*, **121**, 7–23, doi:10.1016/j.pocean.2013.04.002.

Helfrich, K. R., and W. K. Melville, 2006: Long nonlinear internal waves. *Annual Review of Fluid Mechanics*, **38 (1)**, 395–425, doi:10.1146/annurev.fluid.38.050304.092129.

Huang, X., Z. Chen, W. Zhao, Z. Zhang, C. Zhou, Q. Yang, and J. Tian, 2016: An extreme internal solitary wave event observed in the northern South China Sea. *Scientific Reports*, **6 (1)**, 30 041, doi:10.1038/srep30041.

Johnston, T. M. S., 2010: Unpublished dataset from the EXperiment on Internal Tidal Scattering (EXITS), Scripps Institution of Oceanography, University of California.

Johnston, T. M. S., D. L. Rudnick, M. H. Alford, A. Pickering, and H. L. Simmons, 2013: Internal tidal energy fluxes in the South China Sea from density and velocity measurements by gliders. *Journal of Geophysical Research: Oceans*, **118 (8)**, 3939–3949, doi:10.1002/jgrc.20311.

Klymak, J. M., S. Legg, M. H. Alford, M. Buijsman, R. Pinkel, and J. D. Nash, 2012: The direct breaking of internal waves at steep topography. *Oceanography*, **25 (2)**, 150–159, doi:10.5670/oceanog.2012.50.

Klymak, J. M., R. Pinkel, and L. Rainville, 2008: Direct breaking of the internal tide near topography: Kaena Ridge, Hawaii. *Journal of Physical Oceanography*, **38 (2)**, 380 – 399, doi:10.1175/2007JPO3728.1.

Klymak, J. M., and Coauthors, 2006: An estimate of tidal energy lost to turbulence at the Hawaiian Ridge. *Journal of Physical Oceanography*, **36 (6)**, 1148 – 1164, doi:10.1175/JPO2885.1.

Laurent, L. S., and C. Garrett, 2002: The role of internal tides in mixing the deep ocean. *Journal of Physical Oceanography*, **32 (10)**, 2882 – 2899, doi:10.1175/1520-0485(2002)032⟨2882:TROITI⟩2.0.CO;2.

Li, Q., D. Farmer, T. Duda, and S. Ramp, 2009: Acoustical measurement of nonlinear internal waves using the inverted echo sounder. *J. Atmos. Oceanic Technol.*, **26**, doi:10.1175/2009JTECHO652.1.

MacKinnon, J. A., and Coauthors, 2017: Climate process team on internal wave–driven ocean mixing. *Bulletin of the American Meteorological Society*, **98 (11)**, 2429 – 2454, doi:10.1175/BAMS-D-16-0030.1.

Martin, J. P., D. L. Rudnick, and R. Pinkel, 2006: Spatially broad observations of internal waves in the upper ocean at the Hawaiian Ridge. *Journal of Physical Oceanography*, **36**, 1085–1103.

Morozov, E. G., 2018: *Oceanic Internal Tides: Observations, Analysis and Modeling*. 1st ed., Springer Cham.

Munk, W., and C. Wunsch, 1998: Abyssal recipes ii: energetics of tidal and wind mixing. *Deep Sea Research Part I: Oceanographic Research Papers*, **45 (12)**, 1977–2010, doi:10.1016/S0967-0637(98)00070-3.

National Oceanic and Atmospheric Administration (NOAA), 2023: NOAA tide predictions. NOAA, URL https://tidesandcurrents.noaa.gov/tide_predictions.html.

Ostrovsky, L. A., 1978: Nonlinear internal waves in a rotating ocean. *Oceanology*, **18**, 119–125.

Pétrélis, F., S. Llewellyn Smith, and W. R. Young, 2006: Tidal conversion at a submarine ridge. *Journal of Physical Oceanography*, **36 (6)**, 1053 – 1071, doi:10.1175/JPO2879.1.

Rainville, L., and R. Pinkel, 2006: Baroclinic energy flux at the Hawaiian Ridge: Observations from the R/P FLIP. *Journal of Physical Oceanography*, **36 (6)**, 1104 – 1122, doi:10.1175/JPO2882.1.

Ray, R. D., and G. T. Mitchum, 1997: Surface manifestation of internal tides in the deep ocean: observations from altimetry and island gauges. *Progress in Oceanography*, **40 (1)**, 135–162, doi:10.1016/S0079-6611(97)00025-6, tidal Science In Honour of David E. Cartwright.

Rudnick, D. L., and Coauthors, 2003: From tides to mixing along the Hawaiian Ridge. *Science*, **301 (5631)**, 355–357, doi:10.1126/science.1085837.

Simmons, H. L., R. W. Hallberg, and B. K. Arbic, 2004: Internal wave generation in a global baroclinic tide model. *Deep Sea Research Part II: Topical Studies in Oceanography*, **51 (25)**, 3043–3068, doi:10.1016/j.dsr2.2004.09.015, small and mesoscale processes and their impact on the large scale.

Sonmor, L. J., and G. P. Klaassen, 1997: Toward a unified theory of gravity wave stability. *Journal of the Atmospheric Sciences*, **54 (22)**, 2655 – 2680, doi:10.1175/1520-0469(1997)054⟨2655:TAUTOG⟩2.0.CO;2.

Subich, C. J., K. G. Lamb, and M. Stastna, 2013: Simulation of the Navier–Stokes equations in three dimensions with a spectral collocation method. *International Journal for Numerical Methods in Fluids*, **73 (2)**, 103–129, doi:10.1002/fld.3788.

Sutherland, B. R., 2010: *Internal Gravity Waves*. Cambridge University Press, doi:10.1017/CBO9780511780318.

Sutherland, B. R., 2016: Excitation of superharmonics by internal modes in non-uniformly stratified fluid. *Journal of Fluid Mechanics*, **793**, 335–352, doi:10.1017/jfm.2016.108.

Sutherland, B. R., and M. S. Dhaliwal, 2022: The nonlinear evolution of internal tides. Part 1: the superharmonic cascade. *Journal of Fluid Mechanics*, **948**, A21, doi:10.1017/jfm.2022.689.

Sutherland, B. R., and H. Yassin, 2022: The nonlinear evolution of internal tides. Part 2: Lagrangian transport by periodic and modulated waves. *Journal of Fluid Mechanics*, **948**, A22, doi:10.1017/jfm.2022.690.

Vallis, G. K., 2017: *Atmospheric and Oceanic Fluid Dynamics: Fundamentals and Large-Scale Circulation*. 2nd ed., Cambridge University Press, doi:10.1017/9781107588417.

Varma, D., M. Mathur, and T. Dauxois, 2022: Instabilities in internal gravity waves. *Mathematics in Engineering*, **5**, 1–34, doi:10.3934/mine.2023016.

Vic, C., and Coauthors, 2019: Deep-ocean mixing driven by small-scale internal tides. *Nature Communications*, **10 (1)**, 2099, doi:10.1038/s41467-019-10149-5.

Wunsch, C., and R. Ferrari, 2004: Vertical mixing, energy, and the general circulation of the oceans. *Annual Review of Fluid Mechanics*, **36 (1)**, 281–314, doi:10.1146/annurev.fluid.36.050802.122121.

Xie, X., X. Shang, H. van Haren, G. Chen, and Y. Zhang, 2011: Observations of parametric subharmonic instability-induced near-inertial waves equatorward of the critical diurnal latitude. *Geophysical Research Letters*, **38 (5)**, doi:10.1029/2010GL046521.